JOURNAL OF GUIDANCE, CONTROL, AND DYNAMICS
Vol. 30, No. 5, September–October 2007

Relative Angles-Only Navigation and Pose Estimation for Autonomous Orbital Rendezvous

David C. Woffinden* and David K. Geller†
Utah State University, Logan, Utah 84322–1400

DOI: 10.2514/1.28216

The potential of angles-only navigation for autonomous orbital rendezvous is discussed. Flight algorithms for a proposed rendezvous guidance, navigation, and control system are presented. Emphasis is placed on the angles-only navigation filter development to determine relative position and attitude between a passive noncooperative target satellite and a maneuvering chaser vehicle. The navigation filter, a 32-state extended Kalman filter, processes angular measurements from an optical navigation camera along with gyro and star tracker data to estimate the inertial position, velocity, attitude, and angular rates of both vehicles. The filter's performance is evaluated and tested by running a coded prototype in a closed-loop six-degree-of-freedom Monte Carlo simulation containing the various sensors; actuators; guidance, navigation, and control flight algorithms; and dynamics associated with a simple rendezvous scenario. The results include navigation errors, trajectory dispersions, attitude dispersions, and Δv usage. The Monte Carlo results are then compared with linear covariance analysis results and the advantages and potential of each approach are discussed.

I. Introduction

THE ability to rendezvous and dock two spacecraft in orbit has been and will be an essential element of space exploration, particularly in the area of manned spaceflight. The methods and techniques implemented in the past to perform such close-proximity operations often required significant cooperation between both vehicles and had a man in the loop to ensure successful maneuvering of both spacecraft [1]. From a navigational perspective, performing close-proximity maneuvers autonomously previously demanded complex instrumentation requiring additional mass, power, and volume resources. The idea of performing rendezvous maneuvers autonomously without necessitating sophisticated collaboration schemes between vehicles while incorporating lightweight, low-power, compact, navigation sensors has become a sought-after ideal for a variety of missions. This autonomous capability allows for the possibilities of robotic rendezvous and docking missions when ground intervention is impractical or undesirable; future manned missions to reduce the workload on limited human resources; or the servicing and retrieval of a variety of target objects that may be functioning or malfunctioning, alien or familiar, passive or active, cooperative or uncooperative, with or without docking mechanisms. It increases the capability and opportunities to perform rendezvous and docking maneuvers for a variety of scenarios for both large and small spacecraft.

One critical aspect of this problem is developing the capability to autonomously estimate the relative position and velocity between both vehicles, as well as their relative orientations. Although this topic has been addressed [2–8] elsewhere, this paper approaches the problem from a different perspective. First, this paper does not address the crucial and challenging aspect of sensor development or image processing for rendezvous and close-proximity operations. It makes certain assumptions about the performance of the imaging system so that analysis regarding the navigation filter can be evaluated. Second, it is assumed that the target vehicle may be passive or uncooperative and that the navigation equipment required to rendezvous and dock is entirely self-contained with the chaser vehicle. Third, instead of focusing solely on the performance of the navigation filter, this work considers the performance of an angles-only navigation filter as part of an integrated closed-loop guidance, navigation, and control (GNC) system. Fourth, the general orbital and attitude equations of motion are used (i.e., no simplification). Relative navigation is achieved by estimating the inertial position, velocity, attitude, and angular rates of both a target and chaser spacecraft by processing optical line-of-sight (LOS) angles to known target features, gyro data, and star-camera measurements through a 32-state extended Kalman filter.

The objective of this paper is threefold: 1) motivate the potential of angles-only navigation in the context of autonomous orbital rendezvous and close-proximity operations; 2) develop an angles-only navigation filter that can determine the relative position and velocity between two spacecraft, estimate the relative orientation (pose) and angular rates, and support closed-loop proximity operations and maneuvers; and 3) compare the results generated by Monte Carlo simulations to those produced using a linear covariance analysis tool [9] to add validity to the results and highlight the advantages and disadvantages of each method for orbital rendezvous analysis.

II. Notation and Definitions

In this paper, vectors such as position $\boldsymbol{r}$, velocity $\boldsymbol{v}$, angular velocity $\boldsymbol{\omega}$, or state vectors $\boldsymbol{x}$ are shown in bold type. This standard also applies to distinguish between scalar and vector functions. For example, the function defining a single measurement is denoted as $h(\boldsymbol{x})$, where a vector of measurements has the form $\boldsymbol{h}(\boldsymbol{x})$. Vectors with superscripts indicate the coordinate frame representation of the vector. If no superscript is included for a vector, an inertial reference frame is implied. For example, $\boldsymbol{r}$ is the representation of the position vector in the inertial frame and $\boldsymbol{\omega}^b$ is the representation of angular velocity in a body frame. Subscripts are used to provide additional information about the vector. For example, $\boldsymbol{v}_T$ is the representation of the target's velocity vector in the inertial frame, $\boldsymbol{\omega}_c^c$ is the angular velocity of the chaser vehicle in the chaser frame, and $\boldsymbol{x}_P$ is the parameter-state vector.

Matrices are specified by using capital boldface letters, such as $\boldsymbol{P}$ for the state covariance matrix and $\boldsymbol{\Phi}$ for the state transition matrix. Subscripts may be added to clarify any ambiguity or provide additional information. For example, the matrix $\boldsymbol{I}_{n\times n}$ represents the

Presented as Paper 6300 at the AIAA/AAS Astrodynamics Specialist Conference, Keystone, CO, 21–24 August 2006; received 13 October 2006; revision received 16 April 2007; accepted for publication 21 May 2007.

*Ph.D. Candidate, Mechanical and Aerospace Engineering. Student Member AIAA.

†Assistant Professor, Mechanical and Aerospace Engineering. Senior Member AIAA.

identity matrix with n rows and columns, $\boldsymbol{I}_T$ is the moment-of-inertia matrix for the target vehicle, and $\boldsymbol{F}_x$ defines the partial matrix of the state dynamics $\boldsymbol{f}(\boldsymbol{x})$ with respect to the states $\boldsymbol{x}$. A diagonal matrix is written as

$$\text{diag}\,(\boldsymbol{f}) = \begin{bmatrix} f_1 & 0 & 0 \\ 0 & f_2 & 0 \\ 0 & 0 & f_3 \end{bmatrix}$$

A boldface $\boldsymbol{q}$ is reserved for quaternions that are represented by a four-dimensional vector, where the scalar portion of the quaternion is the fourth element.

$$\boldsymbol{q} = \begin{bmatrix} \boldsymbol{u}\sin(\theta/2) \\ \cos(\theta/2) \end{bmatrix}$$

where the unit vector $\boldsymbol{u}$ defines the axis of rotation, and θ is the angle of rotation. The quaternion $\boldsymbol{q}_{I\to C}$ represents the orientation of the chaser reference frame with respect to the inertial frame. The associated direction-cosine matrix (or attitude matrix) is denoted with the capital boldface letter $\boldsymbol{T}$. For example, the transformation from the inertial frame to the chaser frame is given by $\boldsymbol{T}_{I\to C} = \boldsymbol{T}(\boldsymbol{q}_{I\to C})$. The quaternion multiplication operator $\otimes$ is defined such that $\boldsymbol{q}_{a\to c} = \boldsymbol{q}_{b\to c} \otimes \boldsymbol{q}_{a\to b}$ corresponds to the sequence of rotations $\boldsymbol{T}_{a\to c} = \boldsymbol{T}_{b\to c}\boldsymbol{T}_{a\to b}$. Small rotations can be written in terms of quaternions as

$$\delta\boldsymbol{q}(\boldsymbol{\theta}) \approx \begin{bmatrix} \boldsymbol{\theta}/2 \\ 1 \end{bmatrix}$$

or attitude matrices as

$$\delta\boldsymbol{T}(\boldsymbol{\theta}) \approx \boldsymbol{I} - [\boldsymbol{\theta}\times]$$

where $\boldsymbol{\theta} = \theta\boldsymbol{u}$ is a small rotation vector, and $[\boldsymbol{\theta}\times]$ is a cross-product matrix defined by the ordinary cross product $[\boldsymbol{\theta}\times]$, $\boldsymbol{r} = \boldsymbol{\theta} \times \boldsymbol{r}$.

Finally, variables typically have *true* values, *nominal* values, *flight computer* values, and *measured* values. The nominal value of the true variable x will be denoted as $\bar{x}$, the value stored in the flight computer will be denoted as $\hat{x}$, and the measured value will be denoted as $\tilde{x}$.

III. Angles-Only Navigation Potential

The concept of angles-only or bearings-only navigation is not new and has been exploited heavily in the past, particularly in the areas of naval applications [10–12], orbit determination [13,14], and target tracking [15–19]. The same fundamental technique is also the basis for optical navigation, which has played a vital role for lunar [20] and interplanetary missions such as Apollo and various deep space probes [21]. Current and future applications from unmanned-aerial-vehicle (UAV) formation flying [22], autonomous cargo ships to the International Space Station [23], comet and asteroid exploration [24,25], to some lunar landing concepts rely on this strategy. In principle, the idea is simple. By measuring LOS angles (i.e., azimuth and elevation angles) from some reference location to another object of interest, the relative position and velocity between the two objects can be estimated. If the position and velocity of one of the points are known (i.e., a planet's ephemeris), then the position and velocity of the other can theoretically be determined. In reality, there are often subtleties with this method that have resulted in great research efforts to more fully understand the potential and limitations of angles-only navigation.

Although much work has been done in this field, angles-only navigation for rendezvous and docking missions inherits unique challenges not faced in the more conventional applications. First, the relative dynamics and distances of both the observer and target are different. Instead of the observer being at a *fixed* location on land, positioned at sea, or flying in the Earth's atmosphere, it is subject to the dynamics and constraints of the space environment. Also, the relative distance between the observer and target can range between thousands of kilometers to centimeters while performing a variety of possible relative maneuvers. Second, the instruments and techniques ideally suited for measuring these relative angles are also different for rendezvous applications. Traditional methods such as radar may not be the best solution as volume, power consumption, and mass become coveted commodities in space. In fact, it has been argued that for ranges within a few hundred meters, optical sensors provide the best solution for rendezvous navigation when considering performance, mass, power consumption, and complexity [26]. Clearly, readdressing this familiar problem is warranted and has great potential to reveal new insights.

The potential for using *only* angular measurements for rendezvous and docking was recognized from the first rendezvous missions of Gemini [27]. As acknowledged then and reemphasized now, there are two fundamental applications to using an angles-only approach for orbital rendezvous. First, it can be the primary navigation system for cases in which the target is passive or known to be uncooperative. Second, it can also serve in a support role by acting as a backup to a primary navigation system in the event of component failure or performing in conjunction with the primary navigation system to improve performance and mission success.

The potential of angles-only navigation is greatly enhanced when additional information beyond the standard LOS angles, including range and relative attitude information, is obtained from the object's image on the camera focal plane. Suppose the target is spherical in shape, as shown in Fig. 1a. If the size of the target is known, then the relative range ρ can be computed by dividing the known diameter of the target D_{target} by its apparent angular size θ_{target}.

$$\rho = D_{\text{target}}/\theta_{\text{target}} \tag{1}$$

Although the standard line-of-sight angles shown in Fig. 1b are useful, the concept can be extended by taking similar relative observations to various target features, as depicted in Fig. 1c. Depending on the number and location of these features, it has been

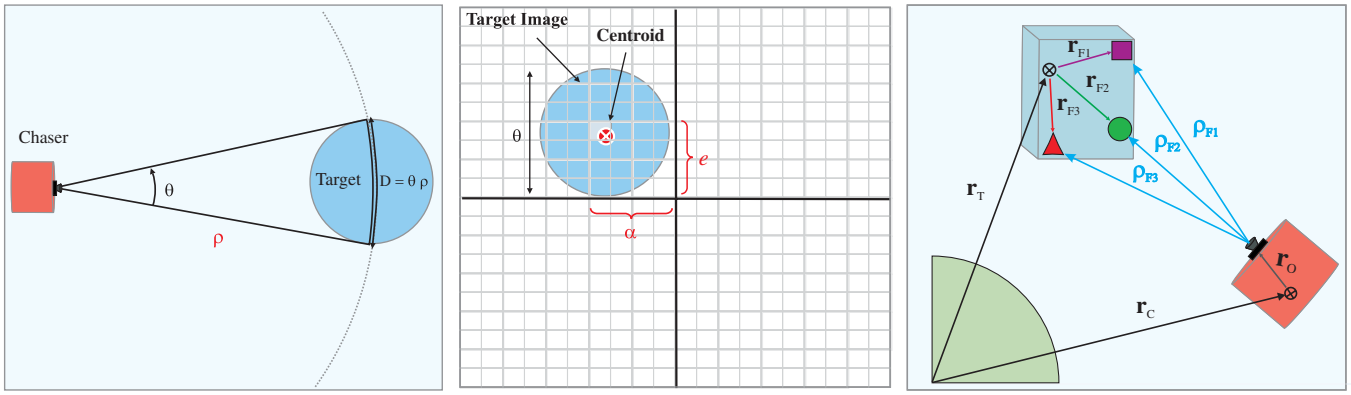

a) Angular range measurement **b) Camera focal plane** **c) Feature measurements**

Fig. 1 Possible angle measurements using an optical navigation camera.

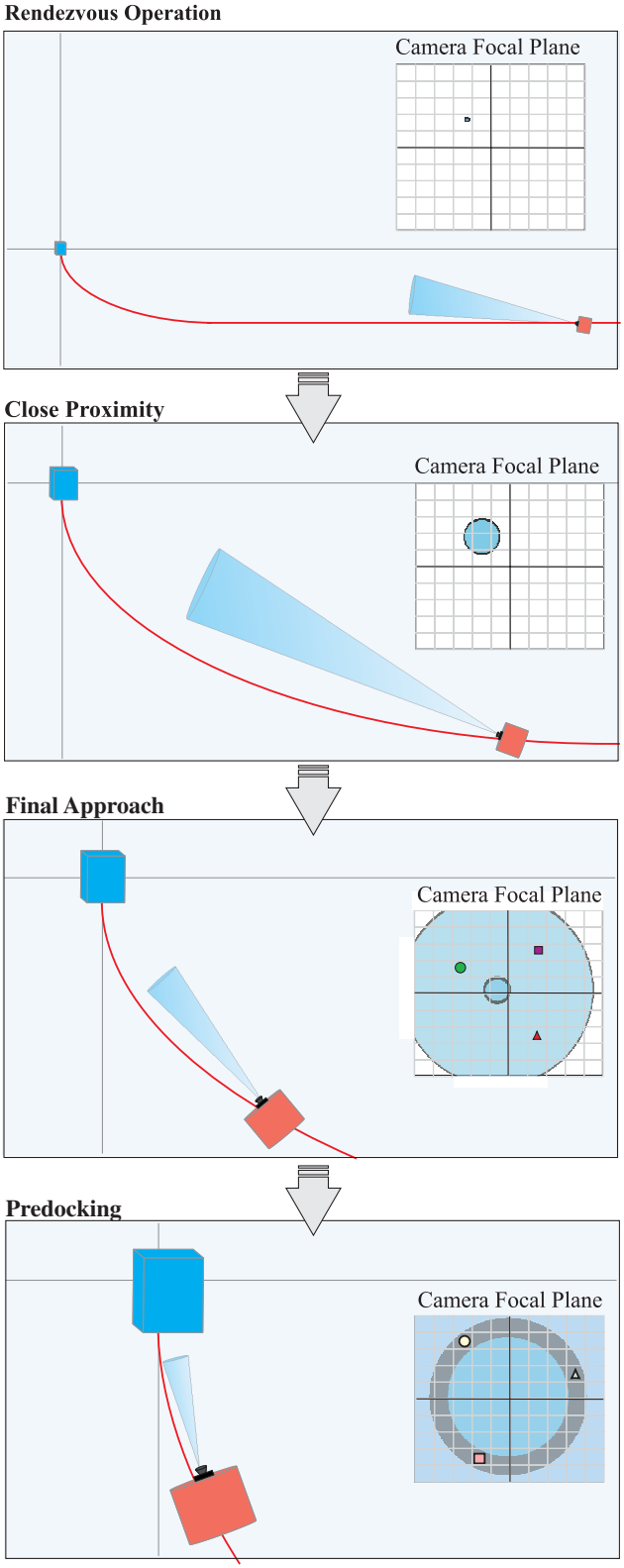

Fig. 2 Terminal rendezvous subphases.

shown [4,9] that relative measurements to key target features can be used to deduce the relative attitude[‡] and range. In fact, by knowing the distance between features, the measured angular separation between them uniquely identifies the relative range between the target and chaser spacecraft [28]. The potential of angles-only navigation increases further when multiple optical navigation cameras (stereoscopic systems) or maneuvers (virtual stereoscopic system) are considered.

As depicted in Fig. 2, the possible angular measurements generated by an optical camera can vary from the moment the chaser first detects the target until docking. There are four potential cases to consider, each defined by the available relative measurements. They include the rendezvous-operation, close-proximity, final-approach, and predocking phases. In each phase, it is assumed that the lighting conditions (either artificially or by proper trajectory selection) are sufficient to ensure reliable angle measurements. The measurement availability associated with each stage depends on a number of mission parameters such as the camera's field of view, pixel resolution, lighting conditions, reflectivity of the target's surface, the size and shape of the target, the number and size of target features, and image-processing capabilities. To formally specify transition indicators from one stage to the next, three specific mission parameters have been selected, including the pixel resolution, camera field of view, and diameter of the target. Of course, these markers are artificial and a more sophisticated approach may be required for specific applications, yet these parameters do provide a general estimate of the anticipated divisions.

Rendezvous-Operation Phase: The chaser vehicle is considered to be in the rendezvous-operation phase when the target is observable on the camera focal plane and the apparent angular diameter of the target's image is less than one pixel θ_{pixel}.

$$\theta_{\text{target}} < \theta_{\text{pixel}}$$

During this period of the mission, the optical camera can track the centroid of the target to generate relative azimuth and elevation measurements.

Close-Proximity Phase: In the close-proximity phase, the chaser vehicle is close enough to the target so that the optical camera can determine the target's apparent angular size. However, it is distanced enough so that the target's image remains within the camera's field of view θ_{FOV}.

$$\theta_{\text{pixel}} < \theta_{\text{target}} < \theta_{\text{FOV}}$$

During this mode of operation, the optical camera can generate three relative measurements to the centroid of the target: azimuth, elevation, and range.

Final-Approach Phase: As the chaser spacecraft advances toward the target, it enters the final-approach phase when the optical camera can identify three or more key features located on the target vehicle and measure the relative azimuth and elevations angles to them. At this point, it is assumed that the target's image overfills the camera's field of view,

$$\theta_{\text{target}} > \theta_{\text{FOV}}$$

eliminating the possibility of determining the azimuth, elevation, and range measurements to the target's centroid.

Predocking Phase: As the chaser prepares for docking, the optical camera can no longer detect the original feature pattern used in the final-approach phase. Having proper alignment with the target vehicle, the optical camera can clearly detect important docking features. During this phase, the optical camera can generate additional azimuth and elevation measurements to docking features or measure the relative azimuth, elevation, and range by identifying the apparent angular size of the docking port.

IV. Rendezvous Simulation

For the orbital rendezvous and close-proximity analyses, a high-fidelity, six-degree-of-freedom, nonlinear simulation tool has been created using MATLAB and Simulink to model the closed-loop dynamics of the rendezvous scenario. There are two primary sections of the simulation: the orbital rendezvous simulation models and the GNC-flight-algorithm models. The simulation models represent the

[‡]It is possible with three features to determine the relative attitude of the target vehicle. However, if the plane of the features is normal to the camera LOS, then a singularity results [7]. A fourth out-of-plane feature will remove the singularity.

actual dynamics of two orbiting spacecraft, the space environment (J_2 gravity model; gravity-gradient torques; random accelerations; and torques to account for drag, solar pressure, higher-order-gravity terms, etc.), sensor measurements, and actuator forces/torques. The GNC flight algorithms consist of the guidance, navigation, and control algorithms necessary to orient and maneuver the chaser spacecraft along the desired rendezvous trajectory.

A. Orbital Rendezvous Simulation Models

The orbital rendezvous simulation models include the chaser and target translational and rotational dynamics; disturbance accelerations and torques; strap-down gyros, star-camera, and optical-navigation-camera measurements; and the torques and velocity changes generated by momentum wheels and thrusters. The truth-model state is a 35-dimensional vector defined by 13 target states $\boldsymbol{x}_T$, 13 chaser states $\boldsymbol{x}_C$, and 9 parameter states associated with various aspects of the sensors used onboard the chaser $\boldsymbol{x}_P$.

$$\boldsymbol{x} = [\boldsymbol{x}_T,\ \boldsymbol{x}_C,\ \boldsymbol{x}_P]^T \tag{2}$$

The 13 target states include the inertial position and velocity vectors, the quaternion defining the orientation of the target with respect to the inertial frame, and the target's angular rate coordinatized in the target vehicle's reference frame.

$$\boldsymbol{x}_T = [\boldsymbol{r}_T,\ \boldsymbol{v}_T,\ \boldsymbol{q}_{I\to T},\ \boldsymbol{\omega}_T^T]^T \tag{3}$$

Similarly, the 13 chaser states are the inertial position and velocity and the inertial-to-body quaternion and its angular rate.

$$\boldsymbol{x}_C = [\boldsymbol{r}_C,\ \boldsymbol{v}_C,\ \boldsymbol{q}_{I\to C},\ \boldsymbol{\omega}_C^C]^T \tag{4}$$

The parameter states are the gyro bias $\boldsymbol{b}_\omega^C$ coordinatized in the chaser frame, the star-camera misalignment $\boldsymbol{\epsilon}_S^S$, and the optical-camera misalignment $\boldsymbol{\epsilon}_0^0$, each referenced in their respective camera frames.

$$\boldsymbol{x}_P = [\boldsymbol{b}_\omega^C,\ \boldsymbol{\epsilon}_S^S,\ \boldsymbol{\epsilon}_O^O]^T \tag{5}$$

These parameter states are modeled as first-order Markov processes with large time constants causing them to behave essentially as biases.

1. Dynamics

The dynamics for the true state vector are

$$\dot{\boldsymbol{r}}_T = \boldsymbol{v}_T \tag{6}$$

$$\dot{\boldsymbol{v}}_T = \boldsymbol{g}_T + \boldsymbol{w}_{g_T} \tag{7}$$

$$\dot{\boldsymbol{q}}_{I\to T} = \tfrac{1}{2}\boldsymbol{\omega}_T^T \otimes \boldsymbol{q}_{I\to T} \tag{8}$$

$$\dot{\boldsymbol{\omega}}_T^T = \boldsymbol{I}_T^{-1}[\boldsymbol{\tau}_g^T - \boldsymbol{\omega}_T^T \times \boldsymbol{I}_T\boldsymbol{\omega}_T^T] + \boldsymbol{w}_{\alpha_T} \tag{9}$$

$$\dot{\boldsymbol{r}}_C = \boldsymbol{v}_C \tag{10}$$

$$\dot{\boldsymbol{v}}_C = \boldsymbol{g}_C + \boldsymbol{w}_{g_C}, \qquad (\boldsymbol{v}_C)^{+c} = (\boldsymbol{v}_C)^{-c} + \boldsymbol{u}_{\Delta v} \tag{11}$$

$$\dot{\boldsymbol{q}}_{I\to C} = \tfrac{1}{2}\boldsymbol{\omega}_C^C \otimes \boldsymbol{q}_{I\to C} \tag{12}$$

$$\dot{\boldsymbol{\omega}}_C^C = \boldsymbol{I}_C^{-1}[\boldsymbol{u}_\tau^C + \boldsymbol{\tau}_g^C - \boldsymbol{\omega}_C^C \times \boldsymbol{I}_C\boldsymbol{\omega}_C^C] + \boldsymbol{w}_{\alpha_C} \tag{13}$$

$$\dot{\boldsymbol{b}}_\omega^C = -\frac{\boldsymbol{b}_\omega^C}{\tau_b} + \boldsymbol{w}_b \tag{14}$$

$$\dot{\boldsymbol{\epsilon}}_S^S = -\frac{\boldsymbol{\epsilon}_S^S}{\tau_S} + \boldsymbol{w}_s \tag{15}$$

$$\dot{\boldsymbol{\epsilon}}_O^O = -\frac{\boldsymbol{\epsilon}_O^O}{\tau_O} + \boldsymbol{w}_o \tag{16}$$

where $\boldsymbol{I}_T$ and $\boldsymbol{I}_C$ are the target and chaser inertia matrices, respectively. The accelerations due to gravity acting on the target and chaser vehicles $\boldsymbol{g}_T$ and $\boldsymbol{g}_C$ are based on the point-mass and J_2 gravity models [29]. The gravity-gradient torques $\boldsymbol{\tau}_g^T$ and $\boldsymbol{\tau}_g^C$ are also derived from point-mass gravity models [29]. The control inputs $\boldsymbol{u}_\tau^C$ and $\boldsymbol{u}_{\Delta v}$ are the torques and impulsive velocity changes executed by the actuators on the chaser spacecraft. The random disturbances $\boldsymbol{w}_{g_T}$, $\boldsymbol{w}_{\alpha_T}$, $\boldsymbol{w}_{g_C}$, and $\boldsymbol{w}_{\alpha_C}$ are included in the models to account for disturbance forces and torques acting on each spacecraft, such as drag, solar-radiation pressure, venting gases, higher-order-gravity-model terms, other celestial bodies, etc. The variances of these uncorrelated white-noise processes are defined as

$$\begin{aligned}
E[\boldsymbol{w}_{g_T}(t)\boldsymbol{w}_{g_T}(t')^T] &= \sigma_{v_T}^2\boldsymbol{I}_{3\times3}\delta(t-t')\\
E[\boldsymbol{w}_{\alpha_T}(t)\boldsymbol{w}_{\alpha_T}(t')^T] &= \sigma_{\omega_T}^2\boldsymbol{I}_{3\times3}\delta(t-t')\\
E[\boldsymbol{w}_{g_C}(t)\boldsymbol{w}_{g_C}(t')^T] &= \sigma_{v_C}^2\boldsymbol{I}_{3\times3}\delta(t-t')\\
E[\boldsymbol{w}_{\alpha_C}(t)\boldsymbol{w}_{\alpha_C}(t')^T] &= \sigma_{\omega_C}^2\boldsymbol{I}_{3\times3}\delta(t-t')
\end{aligned} \tag{17}$$

The process of selecting values for the variances of these disturbances follows a trial-and-error technique outlined by Lear [30], in which the magnitude of the disturbance strength is associated with the expected downrange and attitude error after one orbit. The white-noise terms $\boldsymbol{w}_b$, $\boldsymbol{w}_s$, and $\boldsymbol{w}_o$ drive the first-order Markov processes, modeling the parameter states with variances.

$$\begin{aligned}
E[\boldsymbol{w}_b(t)\boldsymbol{w}_b(t')^T] &= \sigma_b^2\boldsymbol{I}_{3\times3}\delta(t-t')\\
E[\boldsymbol{w}_s(t)\boldsymbol{w}_s(t')^T] &= \sigma_s^2\boldsymbol{I}_{3\times3}\delta(t-t')\\
E[\boldsymbol{w}_o(t)\boldsymbol{w}_o(t')^T] &= \sigma_o^2\boldsymbol{I}_{3\times3}\delta(t-t')
\end{aligned} \tag{18}$$

2. Actuator Models

The simulation contains two actuator models: momentum wheels for attitude control and a system of impulsive thrusters for translational control. The actual torques generated by the momentum wheels for a commanded torque $\hat{\boldsymbol{\tau}}_{\text{cmd}}^C$ includes actuator noise $\boldsymbol{w}_\tau^C$, bias $\boldsymbol{b}_\tau^C$, scale factor biases $\boldsymbol{f}_\tau^C$, and misalignment $\boldsymbol{\epsilon}_\tau^C$.

$$\boldsymbol{u}_\tau^C = \delta\boldsymbol{T}(\boldsymbol{\epsilon}_\tau^C)[\{\boldsymbol{I}_{3\times3} + \text{diag}(\boldsymbol{f}_\tau^C)\}\hat{\boldsymbol{\tau}}_{\text{cmd}}^C + \boldsymbol{b}_\tau^C + \boldsymbol{w}_\tau^C] \tag{19}$$

The covariance of the momentum-wheel noise is $E[\boldsymbol{w}_\tau^C(t)\boldsymbol{w}_\tau^C(t')^T] = \boldsymbol{S}_\tau\delta(t-t')$. The thruster impulsive Δv model also includes error sources such as thruster noise $\boldsymbol{w}_{\Delta v}^C$, biases $\boldsymbol{b}_{\Delta v}^C$, scale factor biases $\boldsymbol{f}_{\Delta v}^C$, and misalignments $\boldsymbol{\epsilon}_{\Delta v}^C$. The covariance of the thruster noise is $E[\boldsymbol{w}_{\Delta v}^C(t_k)\ \ \boldsymbol{w}_{\Delta v}^C(t_{k'})^T] = \boldsymbol{S}_{\Delta v}\delta(t_k - t_{k'})$, such that

$$\boldsymbol{u}_{\Delta v}^C = \boldsymbol{T}(\boldsymbol{q}_{C\to I})\delta\boldsymbol{T}(\boldsymbol{\epsilon}_{\Delta v}^C)[\{\boldsymbol{I}_{3\times3} + \text{diag}(\boldsymbol{f}_{\Delta v}^C)\}\Delta\boldsymbol{v}_{\text{cmd}}^C + \boldsymbol{b}_{\Delta v}^C + \boldsymbol{w}_{\Delta v}^C] \tag{20}$$

where $\Delta\boldsymbol{v}_{\text{cmd}}^C$ is the commanded Δv.

3. Sensor Models

The gyro model is based upon a package of three orthogonal strap-down gyros, each measuring the chaser's angular velocity along its input axis. The measured angular velocity from the gyros is defined as the true angular rate plus gyro bias $\boldsymbol{b}_\omega^C$, scale factor bias $\boldsymbol{f}_\omega^C$, sensor

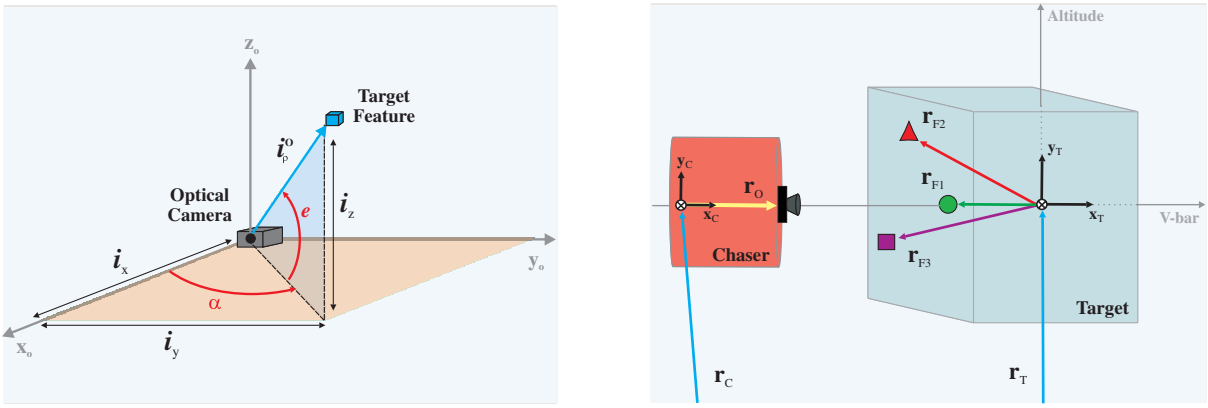

a) Line-of-sight vector and angle measurements

b) Feature Locations

Fig. 3 Relationship between the relative angular measurements and the line-of-sight vector to the target.

noise (angular random walk) $\boldsymbol{v}_\omega^C$, and gyro misalignment $\boldsymbol{\epsilon}_\omega^C$, where the covariance of the gyro noise is $E[\boldsymbol{v}_\omega^C(t_k)\ \ \boldsymbol{v}_\omega^C(t_{k'})^T] = \boldsymbol{S}_\omega \delta(t_k - t_{k'})$.

$$\tilde{\boldsymbol{\omega}}_C^C = \delta \boldsymbol{T}(\boldsymbol{\epsilon}_\omega^C)[\{\boldsymbol{I}_{3\times 3} + \mathrm{diag}(\boldsymbol{f}_\omega^C)\}\boldsymbol{\omega}_C^C + \boldsymbol{b}_\omega^C + \boldsymbol{v}_\omega^C] \tag{21}$$

The star camera is used to measure the three-axis orientation of the chaser vehicle. The model accounts for the uncertainty in the alignment of the star-camera frame $\boldsymbol{\epsilon}_S^S$ with respect to the chaser frame and sensor noise $\boldsymbol{v}_S^S$. The chaser frame referenced throughout the paper refers to the chaser's navigation base. The output of the star-camera model is a quaternion of the form

$$\tilde{\boldsymbol{q}}_{I\to\bar{S}} = \boldsymbol{q}_{S\to\bar{S}} \otimes \boldsymbol{q}_{\bar{S}\to S} \otimes \bar{\boldsymbol{q}}_{C\to S} \otimes \boldsymbol{q}_{I\to C} \tag{22}$$

where $\boldsymbol{q}_{\bar{S}\to S}$ represents the small angular rotation associated with the misalignment of the star camera $\delta\boldsymbol{q}(\boldsymbol{\epsilon}_S^S)$, and $\boldsymbol{q}_{S\to\bar{S}}$ is the angular error due to sensor noise $\delta\boldsymbol{q}(\boldsymbol{\nu}_S^S)$ with the covariance of the measurement noise $\boldsymbol{v}_S^S$ given by

$$E[\boldsymbol{v}_S^S(t_k)\ \ \boldsymbol{v}_S^S(t_{k'})^T] = \boldsymbol{R}_S \delta_{kk'}$$

The optical-tracking camera is used by the chaser to image and track the target's centroid or known target features. It has a field of view of 30 deg with a focal plane of 1000 pixels, such that the pixel resolution is three-hundredths of a degree or half of a milliradian. The model contains an uncertainty in the alignment of the optical-tracking-camera frame with respect to the chaser frame $\boldsymbol{\epsilon}_O^O$, in addition to sensor noise ν. There are undoubtedly additional error sources, such as distortion in the camera lens or shadowing effects, that are not included in this model but could be explored further. The effects of pixelation are removed by ensuring that the sum of the measurement errors and noise exceeds the pixel size. The optical camera effectively provides line-of-sight information (i.e., azimuth and elevation angles) by measuring the feature pixel location in the camera focal plane. The azimuth and elevation measurements $\tilde{\alpha}$ and $\tilde{e}$ from the optical tracking camera[§] are given by

$$\tilde{\alpha} = \tan^{-1}\left(\frac{i_y}{i_x}\right) + \nu_\alpha \tag{23}$$

$$\tilde{e} = \sin^{-1}(i_z) + \nu_e \tag{24}$$

where $[i_x\ \ i_y\ \ i_z]^T$ are the individual components of the relative line-of-sight unit vector $\boldsymbol{i}_\rho^O$ between the optical camera and the target (or target features) represented in the optical frame. This unit vector can be written in terms of the noise-free angle measurements α and e as

$$\boldsymbol{i}_\rho^O = \begin{bmatrix} \cos(e)\cos(\alpha) \\ \cos(e)\sin(\alpha) \\ \sin(e) \end{bmatrix} \tag{25}$$

depicted in Fig. 3a. The relative range unit vector can also be expressed in terms of the true states.

$$\boldsymbol{i}_\rho^O = [\delta \boldsymbol{T}(\boldsymbol{\epsilon}_O^O)\boldsymbol{T}_{c\to\tilde{o}}\boldsymbol{T}(\boldsymbol{q}_{I\to C})]\left[\frac{\{\boldsymbol{r}_T + \boldsymbol{T}(\boldsymbol{q}_{T\to I})\boldsymbol{r}_F^T\} - \{\boldsymbol{r}_C + \boldsymbol{T}(\boldsymbol{q}_{C\to I})\boldsymbol{r}_O^C\}}{|\{\boldsymbol{r}_T + \boldsymbol{T}(\boldsymbol{q}_{T\to I})\boldsymbol{r}_F^T\} - \{\boldsymbol{r}_C + \boldsymbol{T}(\boldsymbol{q}_{C\to I})\boldsymbol{r}_O^C\}|}\right] \tag{26}$$

where the feature position in the target frame $\boldsymbol{r}_F^T$ and the optical-tracking-camera position in the chaser frame $\boldsymbol{r}_O^C$ are indicated in Fig. 3b. By defining the optical-camera-noise vector $\boldsymbol{v}_O^O = [\nu_\alpha\ \ \nu_e]^T$, the covariance of the camera-measurement noise becomes

$$E[\boldsymbol{v}_O^O(t_k)\ \ \boldsymbol{v}_O^O(t_{k'})^T] = \boldsymbol{R}_O \delta_{kk'}$$

B. GNC Flight Algorithms

For relative navigation and pose estimation, it is debatable whether to use relative states (i.e., relative position and velocity) to limit the size of the navigation filter versus the inertial states (i.e., the inertial position and velocity of both vehicles) to maximize the available information. The selected navigation states for the prototype filter is a 32-state vector

$$\hat{\boldsymbol{x}} = [\hat{\boldsymbol{x}}_T,\ \ \hat{\boldsymbol{x}}_C,\ \ \hat{\boldsymbol{x}}_P]^T \tag{27}$$

consisting of 13 target states, 10 chaser states, and 9 parameter states.

$$\hat{\boldsymbol{x}}_T = [\hat{\boldsymbol{r}}_T,\ \ \hat{\boldsymbol{v}}_T,\ \ \hat{\boldsymbol{q}}_{I\to T},\ \ \hat{\boldsymbol{\omega}}_T^T]^T \tag{28}$$

$$\hat{\boldsymbol{x}}_C = [\hat{\boldsymbol{r}}_C,\ \ \hat{\boldsymbol{v}}_C,\ \ \hat{\boldsymbol{q}}_{I\to C}]^T \tag{29}$$

$$\hat{\boldsymbol{x}}_P = [\hat{\boldsymbol{b}}_\omega^C,\ \ \hat{\boldsymbol{\epsilon}}_S^S,\ \ \hat{\boldsymbol{\epsilon}}_O^O]^T \tag{30}$$

This approach attempts to capture all the available information related to the estimation process to serve as a benchmark for the filter's performance and identify key characteristics that may be overlooked when using a reduced navigation state. Note that the chaser state does not contain angular velocity, because the attitude model (given next) operates in model-replacement mode [31], in which gyro measurements replace the Euler equations that would otherwise model the dynamics of the angular velocity state. For the target, this is not the case, because target gyro data is unavailable.

[§]When focal-plane measurements are generated by the optical navigation system and not angular measurements, see [31] for the measurement equation and measurement partial derivation.

1. Navigation

The angles-only-rendezvous navigation filter is an extended Kalman filter that processes angular measurements to three observable target features using an optical navigation camera and attitude data from gyros and a star camera. The dynamic models used to propagate the navigation states are

$$\dot{\hat{\boldsymbol{r}}}_T = \hat{\boldsymbol{v}}_T \tag{31}$$

$$\dot{\hat{\boldsymbol{v}}} = \hat{\boldsymbol{g}}_T \tag{32}$$

$$\dot{\hat{\boldsymbol{q}}}_{I\to T} = \tfrac{1}{2}\hat{\boldsymbol{\omega}}_T^T \otimes \hat{\boldsymbol{q}}_{I\to T} \tag{33}$$

$$\dot{\hat{\boldsymbol{\omega}}}_T^T = \hat{\boldsymbol{I}}_T^{-1}[\hat{\boldsymbol{\tau}}_g^T - \hat{\boldsymbol{\omega}}_T^T \times \hat{\boldsymbol{I}}_T\hat{\boldsymbol{\omega}}_T^T] \tag{34}$$

$$\dot{\hat{\boldsymbol{r}}}_C = \hat{\boldsymbol{v}}_C \tag{35}$$

$$\dot{\hat{\boldsymbol{v}}}_C = \hat{\boldsymbol{g}}_C + \hat{\boldsymbol{u}}_{\Delta v} \tag{36}$$

$$\dot{\hat{\boldsymbol{q}}}_{I\to C} = \tfrac{1}{2}(\tilde{\boldsymbol{\omega}}_C^C - \hat{\boldsymbol{b}}_\omega^C) \otimes \hat{\boldsymbol{q}}_{I\to C} \tag{37}$$

$$\dot{\hat{\boldsymbol{b}}}_\omega^C = -\frac{\hat{\boldsymbol{b}}_\omega^C}{\tau_b} \tag{38}$$

$$\dot{\hat{\boldsymbol{\epsilon}}}_S^S = -\frac{\hat{\boldsymbol{\epsilon}}_S^S}{\tau_S} \tag{39}$$

$$\dot{\hat{\boldsymbol{\epsilon}}}_O^O = -\frac{\hat{\boldsymbol{\epsilon}}_O^O}{\tau_O} \tag{40}$$

where the accelerations due to gravity on the target and chaser vehicles $\hat{\boldsymbol{g}}_T$ and $\hat{\boldsymbol{g}}_C$ are point-mass and J_2 gravity models [29]. The gravity-gradient torque $\hat{\boldsymbol{\tau}}_g^T$ acting on the target vehicle is based on point-mass models [32]. For the prototype filter, the states are propagated by integrating the nonlinear models using a fourth-order Runge–Kutta integration technique. Because of covariance singularities associated with the use of quaternions [33], a modified state vector is adopted to propagate the covariance matrix and used to update both the states and the covariance matrix. The modified state vector replaces the four-dimensional quaternion states $\hat{\boldsymbol{q}}_{I\to T}$ and $\hat{\boldsymbol{q}}_{I\to C}$ with the three-dimensional rotation vectors $\hat{\boldsymbol{\theta}}_T^T$ and $\hat{\boldsymbol{\theta}}_C^C$. Consequently, the quaternion kinematics are also replaced using the Bortz equation [31]. Thus, the quaternion errors $\delta\boldsymbol{q}$ are replaced by the three-dimensional small-angle rotation vectors $\delta\boldsymbol{\theta}$, and the linearized Bortz equation is used to derive the attitude-covariance propagation equations [31]. As a result, the 32-dimensional navigation state is converted into a 30-dimensional modified state vector $\hat{\boldsymbol{m}}$. The covariance matrix stored on the flight computer, $\hat{\boldsymbol{P}}$, is propagated forward using the linear equation.

$$\hat{\boldsymbol{P}} = \hat{\boldsymbol{\Phi}}\hat{\boldsymbol{P}}_0\hat{\boldsymbol{\Phi}}^T + \hat{\boldsymbol{Q}}_w + \hat{\boldsymbol{Q}}_\eta \tag{41}$$

where $\hat{\boldsymbol{\Phi}}$ is the state transition matrix, $\hat{\boldsymbol{P}}_0$ is the *initial* covariance matrix at time t_0, $\hat{\boldsymbol{Q}}_w$ is the state process-noise covariance matrix, and $\hat{\boldsymbol{Q}}_\eta$ is the flight computer's value of the gyro-process-noise covariance matrix. Using the modified navigation-state vector, the exact expressions of these key variables in terms of the state partial derivatives $\hat{\boldsymbol{F}}$ and the *strength* of state process noise $\hat{\boldsymbol{S}}_w$ and gyro random angular walk $\hat{\boldsymbol{S}}_\eta$ are given in the Appendix [Eqs. (A1), (A6), and (A10)]. When measurements are available, the modified states and the state covariance matrix are updated using the fundamental update equations.

$$\hat{\boldsymbol{m}}^+ = \hat{\boldsymbol{m}}^- + \hat{\boldsymbol{K}}(\tilde{\boldsymbol{z}} - \hat{\boldsymbol{z}}) \tag{42}$$

$$\hat{\boldsymbol{P}}^+ = (\boldsymbol{I} - \hat{\boldsymbol{K}}\hat{\boldsymbol{H}})\hat{\boldsymbol{P}}^- \tag{43}$$

where $\hat{\boldsymbol{K}} = \hat{\boldsymbol{P}}^-\hat{\boldsymbol{H}}^T(\hat{\boldsymbol{H}}\hat{\boldsymbol{P}}^-\hat{\boldsymbol{H}}^T + \hat{\boldsymbol{R}})^{-1}$ is the Kalman gain, and the superscript minus and plus signs indicate the time period just before and after the measurement updates. All of the updated navigation states except the attitude states are contained in the new modified state vector. The quaternions defining the target and chaser orientation are updated using the small rotation vectors.

$$\hat{\boldsymbol{q}}_{I\to T}^+ = \delta\boldsymbol{q}(\hat{\boldsymbol{\theta}}_T^T) \otimes \hat{\boldsymbol{q}}_{I\to T}^- \qquad \hat{\boldsymbol{q}}_{I\to C}^+ = \delta\boldsymbol{q}(\hat{\boldsymbol{\theta}}_C^C) \otimes \hat{\boldsymbol{q}}_{I\to C}^-$$

The measurement equations used by the flight computer to estimate the various measurements $\hat{\boldsymbol{z}}$ are presented in Sec. A.II of the Appendix, along with the associated measurement sensitivity matrix $\hat{\boldsymbol{H}}$ and the measurement covariance matrix $\hat{\boldsymbol{R}}$. Finally, when an impulsive Δv maneuver is used to correct the chaser's velocity, a correction must be made to the navigation-state and covariance matrices.

$$(\hat{\boldsymbol{v}}_C)^{+c} = (\hat{\boldsymbol{v}}_C)^{-c} + \hat{\boldsymbol{u}}_{\Delta v} \tag{44}$$

$$\hat{\boldsymbol{P}}^{+c} = (\boldsymbol{I} + \hat{\boldsymbol{D}})\hat{\boldsymbol{P}}^{-c}(\boldsymbol{I} + \hat{\boldsymbol{D}})^T + \hat{\boldsymbol{S}}_{\Delta v} \tag{45}$$

Once again, the superscript $-c$ and $+c$ signs indicate the time period just before and after the instantaneous corrective maneuver. The estimated velocity change is computed as

$$\hat{\boldsymbol{u}}_{\Delta v} = \boldsymbol{T}(\hat{\boldsymbol{q}}_{C\to I})\Delta\hat{\boldsymbol{v}}_{\text{cmd}}^C \tag{46}$$

The partial derivative $\hat{\boldsymbol{D}}$, representing the additional error introduced because of the maneuver, is given in Sec. A.III of the Appendix, and the thruster noise covariance $\hat{\boldsymbol{S}}_{\Delta v}$ is defined earlier in this section.

2. Guidance

In this discussion, the term *guidance* refers to the algorithms that specify the desired position and velocity of the chaser vehicle and its desired orientation and angular velocity during the given rendezvous scenario. The desired trajectory is specified by the nominal position of the chaser's attach point $\boldsymbol{r}_{\text{attach}}^C$ (colocated with the optical camera $\boldsymbol{r}_O^C$) relative to a docking port location on the target $\boldsymbol{r}_{\text{dock}}^T$ (defined as feature 1, $\boldsymbol{r}_{F1}^T$) as a function of time. The desired position and velocity of the chaser's center of mass is given by

$$\hat{\boldsymbol{r}}_{\text{des}} = \hat{\boldsymbol{r}}_T + \boldsymbol{T}(\hat{\boldsymbol{q}}_{T\to I})[\hat{\boldsymbol{r}}_{\text{dock}}^T + \boldsymbol{T}(\hat{\boldsymbol{q}}_{D\to T})\hat{\boldsymbol{r}}_{\text{rel-des}}^D] - \boldsymbol{T}(\hat{\boldsymbol{q}}_{C\to I})\hat{\boldsymbol{r}}_{\text{attach}}^C \tag{47}$$

$$\hat{\boldsymbol{v}}_{\text{des}} = \hat{\boldsymbol{v}}_T + \boldsymbol{T}(\hat{\boldsymbol{q}}_{T\to I})\{\boldsymbol{T}(\hat{\boldsymbol{q}}_{D\to T})\hat{\boldsymbol{v}}_{\text{rel-des}}^D + \hat{\boldsymbol{\omega}}_T^T \times [\hat{\boldsymbol{r}}_{\text{dock}}^T + \boldsymbol{T}(\hat{\boldsymbol{q}}_{D\to T})\hat{\boldsymbol{r}}_{\text{rel-des}}^D]\} - \boldsymbol{T}(\hat{\boldsymbol{q}}_{C\to I})(\hat{\boldsymbol{\omega}}_{\text{des}}^C \times \hat{\boldsymbol{r}}_{\text{attach}}^C) \tag{48}$$

where $\hat{\boldsymbol{r}}_{\text{rel-des}}^D$ and $\hat{\boldsymbol{v}}_{\text{rel-des}}^D$ are the desired position and velocity of the chaser's attach point $\hat{\boldsymbol{r}}_{\text{attach}}^C$ relative to the rotating docking port frame. At short ranges (less than 100 m) when the chaser approaches the target for inspection, berthing, and/or docking, the desired attitude and angular rate of the chaser is specified to match the attitude and angular rate of the target.

$$\hat{\boldsymbol{q}}_{\text{des}} = \hat{\boldsymbol{q}}_{I\to T} \tag{49}$$

$$\hat{\boldsymbol{\omega}}^{C}_{\text{des}} = \boldsymbol{T}(\hat{\boldsymbol{q}}_{T\to C})\hat{\boldsymbol{\omega}}^{T}_{T} \tag{50}$$

The desired position and velocity commands direct the chaser to approach the target along the target's x axis (docking port axis) and the attitude/attitude-rate-matching technique ensures that the camera is pointing toward the target features at all times. This specialized strategy is valid for either a final-approach trajectory for docking or an inspection-and-hold approach aimed to track a particular area of the target.

3. Control

For close-in proximity operations such as inspection and docking, a proportional–derivative (PD) controller is employed for both the rotational and translational control. The translational control algorithm computes the required $\Delta\boldsymbol{v}$ to track the desired trajectory specified by the *guidance* algorithms in Eqs. (47) and (48).

$$\Delta\hat{\boldsymbol{v}}_{\text{rqd}} = \boldsymbol{K}_r(\hat{\boldsymbol{r}}_{\text{des}} - \hat{\boldsymbol{r}}_C) + \boldsymbol{K}_v(\hat{\boldsymbol{v}}_{\text{des}} - \hat{\boldsymbol{v}}_C) \tag{51}$$

The commanded $\Delta\boldsymbol{v}$ issued to the actuators is the required $\Delta\boldsymbol{v}$ transformed to the chaser frame.

$$\Delta\hat{\boldsymbol{v}}_{\text{cmd}} = \boldsymbol{T}(\hat{\boldsymbol{q}}_{I\to C})\Delta\hat{\boldsymbol{v}}_{\text{rqd}} \tag{52}$$

The commanded torques for the chaser spacecraft to match its orientation with the target vehicle are computed as

$$\hat{\boldsymbol{\tau}}^{C}_{\text{cmd}} = \boldsymbol{K}_\theta(\boldsymbol{\theta}^{C}_{\text{des}}) + \boldsymbol{K}_\omega(\hat{\boldsymbol{\omega}}^{C}_{\text{des}} - \hat{\boldsymbol{\omega}}^{C}_{C}) \tag{53}$$

where the desired angular offset $\boldsymbol{\theta}^{C}_{\text{des}}$ is the angular *difference* between the desired attitude quaternion for the chaser $\hat{\boldsymbol{q}}_{\text{des}}$ and its current attitude $\hat{\boldsymbol{q}}_{I\to c}$.

$$\begin{bmatrix}\boldsymbol{\theta}^{C}_{\text{des}}\\ 1\end{bmatrix} = \hat{\boldsymbol{q}}_{\text{des}} \otimes \hat{\boldsymbol{q}}_{C\to I} \tag{54}$$

V. Rendezvous Analysis

The ultimate objective of this analysis is twofold. First, evaluate the performance of the prototype angles-only navigation filter. Second, determine the performance of the entire closed-loop relative position and attitude control system while implementing the angles-only navigation filter in a rendezvous and close-proximity scenario. The rendezvous analysis is conducted using a standard Monte Carlo simulation method and then compared with results [9] generated by a linear covariance (LinCov) analysis program [34]. Both approaches contain their strengths and weaknesses, but combined, they provide a unique analysis package.

The rendezvous GNC Monte Carlo simulation, as presented in Sec. IV, is depicted in Fig. 4. Flight-computer-actuator commands and white-noise processes drive truth models, which in turn generate the true state $\boldsymbol{x}$ of the system and simulated sensor measurements. The navigation algorithm processes the sensor data and produces a navigation state $\hat{\boldsymbol{x}}$ and a navigation-state error covariance $\hat{\boldsymbol{P}}$. The navigation state is used by the guidance and control functions of the flight computer to generate the actuator commands. The key variables are the *true dispersions* from the reference $\delta\boldsymbol{x} = \boldsymbol{x} - \bar{\boldsymbol{x}}$ and the *true navigation errors* $\delta\boldsymbol{e} = \boldsymbol{x} - \hat{\boldsymbol{x}}$.

In a Monte Carlo program, the covariance of the dispersions and navigation errors are determined by collecting and compiling the results of N simulations.

$$\boldsymbol{D}_{\text{true}} \approx \frac{1}{N-1}\sum_{i=1}^{N}\delta\boldsymbol{x}\delta\boldsymbol{x}^T \qquad \boldsymbol{P}_{\text{true}} \approx \frac{1}{N-1}\sum_{i=1}^{N}\delta\boldsymbol{e}\delta\boldsymbol{e}^T \tag{55}$$

The covariance of trajectory and attitude dispersions, navigation errors, and Δv or fuel usage is often of primary interest. Navigation performance is determined by evaluating and comparing $\boldsymbol{P}_{\text{true}}$ and $\hat{\boldsymbol{P}}$. In a linear covariance approach, the covariances in Eq. (55) are generated in a single simulation by directly propagating, updating, and correcting an *augmented* state covariance matrix.

The LinCov program is ideal for a top-level analysis because it will produce Monte Carlo-like results in a fraction of the time. However, it has its limitations. Although it can characterize the performance of the navigation system and its affects in a closed-loop GNC environment, it does not represent the actual performance of a specific navigation filter in the same setting. It does not generate or process measurements. It does not produce actual control torques or Δv maneuvers. It only produces the statistical results based on a linearized version of the Monte Carlo simulation. As a consequence, there may be subtleties such as nonlinearities, approximations made in the filter design, or even flaws with the filter itself that could not be detected. This is where the Monte Carlo technique has its advantages. It is true that long simulation runs may be required, but a more realistic evaluation of a particular filter's performance in a more *missionlike* environment can be obtained. It also allows an analysis of various intricacies of the filter, flight algorithms, sensor models, or actuator models. The linear covariance analysis provides the big-picture view of the problem. Depending on the design phase, one technique may prove more applicable and relevant than the other. However, both offer complementary results and can serve as a natural checks-and-balance tool throughout the complete design and analysis cycle.

A simple rendezvous and docking scenario serves to test the performance of the proposed relative navigation filter. Using 200 Monte Carlo runs, the prototype angles-only navigation filter is analyzed. The results not only include the relative position and attitude navigation errors, but reveal the relative trajectory

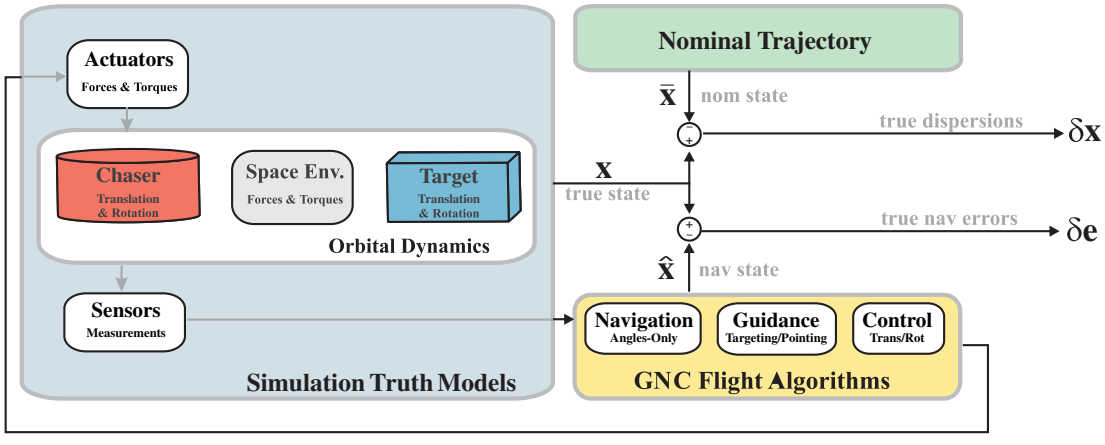

Fig. 4 Monte Carlo simulation for GNC analysis.

dispersions of the closed-loop GNC system. The rendezvous scenario duplicates a similar close-proximity reference mission analyzed using linear covariance analysis [9] and the two results are compared.

A. Reference Mission and Trajectory

The chaser and target are in low-Earth near-circular orbits. The target is in a passive local-vertical/local-horizontal (LVLH) orientation and the chaser is actively controlling its relative attitude and position. The chaser is initially 25 m behind the object on the local-horizontal (v-bar) axis and begins a 2 cm/s approach along the target's body x axis which is nominally aligned with the local-horizontal axis. The approach takes approximately 20 min until the tracking camera is about 1 m from the target's docking port. Nominal minimum impulses of 5 mm/s occur approximately every 100 s or every 2 m, primarily in a negative-altitude direction to maintain the chaser on the v-bar during the final approach. The total accumulated Δv for this nominal approach is 7.3 cm/s, with a 3σ value of 81 cm/s using linear covariance analysis and 127 cm/s statistical 3σ value based on Monte Carlo analysis.

As depicted in Fig. 3b, the optical camera is located 1 m from the chaser's center of mass in the direction of the positive body x axis (toward the target) and colocated with the chaser's attachment point $\boldsymbol{r}^C_{\text{attach}}$. A docking port $\boldsymbol{r}^T_{\text{dock}}$ is located 0.8 m from the target's center of mass in the direction of the negative body x axis (toward the chaser) and colocated with feature 1. Feature 2 is located 20 cm in front of the docking port $\boldsymbol{r}^T_{\text{dock}}$ in the negative body x axis and up 20 cm in the body y axis. Feature 3 is also located 20 cm from $\boldsymbol{r}^T_{\text{dock}}$ in the negative body x-axis direction but 20 cm *out* in the positive body z axis.

The chaser's flight computer processes discrete star-camera measurements every 10 s and continuous strap-down gyro data. Relative navigation is achieved by tracking the three target features (known to a 3σ accuracy of 1 cm) with the optical navigation camera and processing the line-of-sight angular measurements every 60 s. Translational control is achieved with short maneuvers modeled as impulsive burns, and attitude control is achieved with momentum wheels. The model parameters and initial conditions for both the Monte Carlo and linear covariance analysis are shown in Table 1.

B. Relative Navigation Analysis

The relative navigation performance is presented in Fig. 5. The magnitude and LVLH components of the 3σ relative position error are shown at the top of the figure. The magnitude and components of the 3σ relative attitude error in the chaser body frame are shown with the lower plots. Note that the data for the magnitudes of the 3σ relative position and attitude errors are plotted as a function of the chaser's center of mass relative downrange distance to the target's centers of mass. At the end of the simulation, the range between centers of mass is 3 m, and the distance between the optical tracking camera and the target features is only 1 m. The components of the relative navigation errors are plotted as a function of time.

As seen from the relative position plots in Fig. 5, the total relative position navigation error is dominated by the downrange component. After the first few optical camera measurements, the statistical 3σ errors in cross-track and altitude drop from their initial 5 m values to 15 cm and gradually decrease to 4 cm when the two vehicles are 3 m apart. The LinCov 3σ results are very similar to the statistical results, with the final cross-track and altitude 3σ errors being slightly more than 2 cm. The downrange element does not have such a drastic initial change. However, as the chaser approaches the target, the downrange position error appears to drop proportionally to the range to a final 3σ statistical value of 6 cm. Again, the LinCov results followed very similar trends, with the final downrange 3σ position error being slightly less at about 4 cm. At the end of the scenario when the two vehicles are 3 m apart, the total 3σ relative position error is approximately 9 cm from the Monte Carlo analysis and about 5 cm according to the LinCov tool. Besides the initial transient phase, the linear covariance analysis matches up nicely with the Monte Carlo results.

Table 1 Initial condition, disturbance, control, sensor, and actuator parameters for the Monte Carlo simulation and linear covariance analyses

		Monte Carlo	Linear covariance
Initial condition error 3-σ			
Attitude and attitude-rate navigation/dispersion error	per axis	0.1 rad, 0.1 mrad/s	0.1 rad, 0.1 mrad/s
Position and velocity navigation/dispersion error	per axis	3 m, 3 mm/s	3 m, 3 mm/s
Unmodeled disturbances 3-σ			
Rotational disturbances	per axis	0.001 mrad/s/$\sqrt{\text{s}}$ (10 deg/orbit)	0.001 mrad/s/$\sqrt{\text{s}}$ (10 deg/orbit)
Translational disturbances	downrange	0.06 mm/s/$\sqrt{\text{s}}$ (100 m/orbit)	0.06 mm/s/$\sqrt{\text{s}}$ (100 m/orbit)
Control parameters			
Rotational natural frequency and damping ratio	$1/\omega_n$, δ	30 s, 0.7	30 s, 0.7
Translational natural frequency and damping ratio	$1/\omega_n$, δ	200 s, 0.7	200 s, 0,7
Sensor error 3-σ			
Gyro error	drift rate	3.0 deg/h/axis	3.0 deg/h/axis
	scale factor	300 ppm/axis	300 ppm/axis
	misalignment	3 mrad/axis	3 mrad/axis
	random walk	0.05 mrad/$\sqrt{\text{s}}$	0.05 mrad/$\sqrt{\text{s}}$
Star camera error	misalignment	1 mrad/axis	1 mrad/axis
	noise	1 mrad/axis	1 mrad/axis
	measurements	$\Delta t = 10$ s	$\Delta t = 10$ s
Optical tracking camera error	misalignment	1 mrad/axis	1 mrad/axis
	noise	1 mrad/axis	1 mrad/axis
	measurements	$\Delta t = 60$ s	$\Delta t = 60$ s
	feature location error	1 cm	1 cm
Actuator error 3-σ			
Maneuver execution error	directional	1 mrad/axis	1 mrad/axis
	bias	0.1 mm/s	1 mm/s
	scale factor	1000 ppm	1000 ppm
	random	1 mm/s	1 mm/s
	min impulse	5 mm/s	5 mm/s
Torque execution error	directional	1 mrad/axis	1 mrad/axis
	bias	0.1 mN · mm	0.1 mN · mm
	scale factor	1000 ppm	1000 ppm

The Monte Carlo and LinCov analyses for the relative position shows that as the chaser approaches the target along the v-bar, the angle measurements to the target immediately reduce the navigation errors in the relative cross-track and altitude but gradually eliminates the downrange component. This behavior is due to the geometry of the problem. At large enough distances, getting angle measurements to three or more target features is similar to getting a single angle measurement to the target's center of mass, because the separation between features cannot be distinguished. These measurements are able to detect deviations in the cross-track and altitude motion, but it becomes difficult to determine range. It is not until the chaser approaches more closely to the target that the angular separation between the target features can be adequately detected, which directly corresponds to the relative distance separating the two vehicles. Because the optical camera is able to distinguish the feature locations, the navigation filter is able to more precisely determine the downrange position of the chaser. In fact, the improvement in the downrange estimate is proportional to the inverse of the relative range.

The initial relative attitude uncertainty is approximately 15 deg 3σ. At the final downrange position, for which the relative distance between the optical camera and the target docking port is 1 m, there is approximately a 3σ statistical relative attitude error of about 1 deg in the chaser's x axis, 1.5 deg in the y axis, and 1.3 deg in the z axis. The total magnitude of the final 3σ relative attitude navigation errors is about 2.2 deg for the Monte Carlo results and 2 deg for the LinCov results.

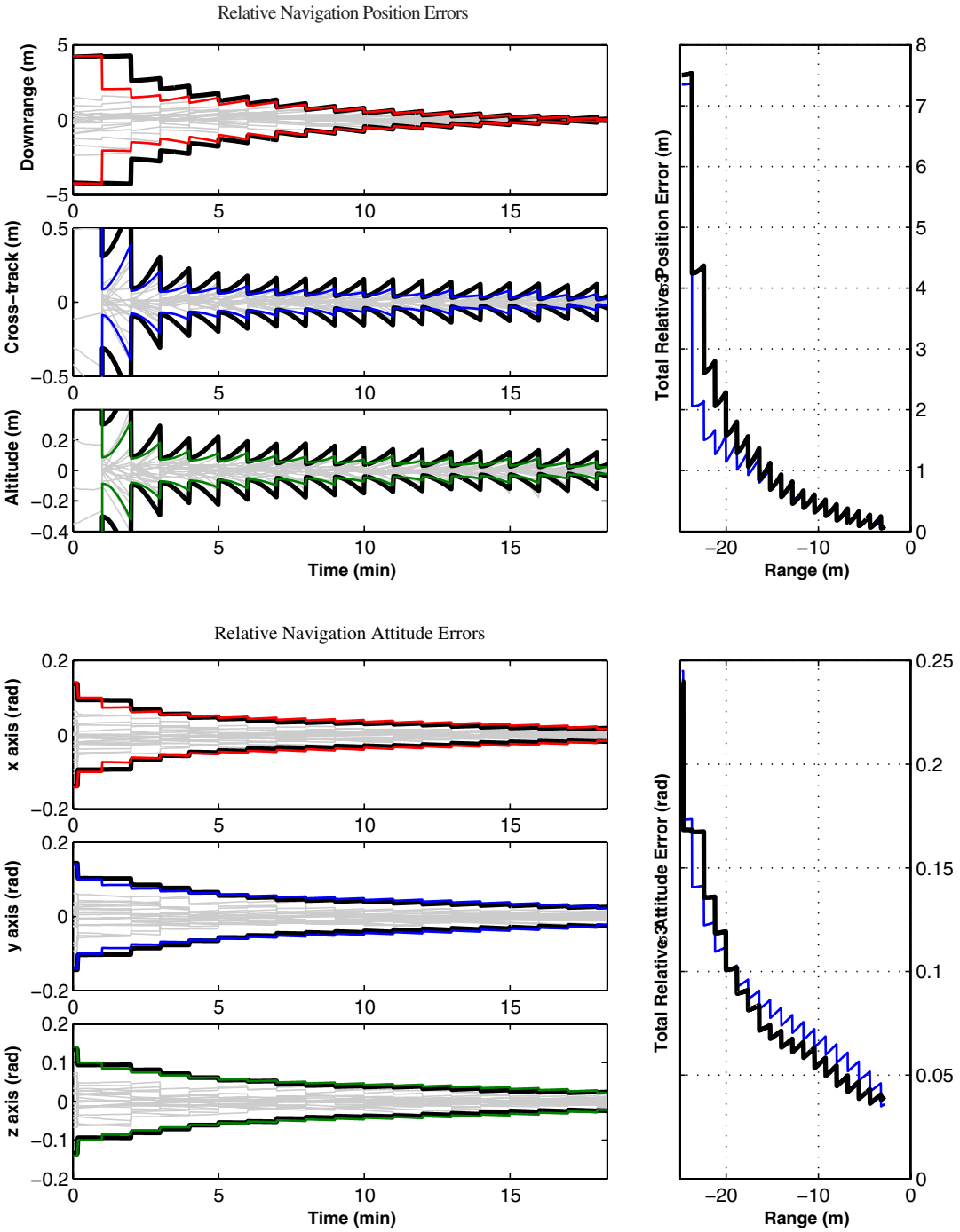

Fig. 5 Relative navigation position errors in LVLH coordinates and relative attitude errors in the chaser frame. The 3σ statistical results from 200 Monte Carlo simulations are shown with thick black lines, and the 3σ navigation errors generated by the LinCov tool are displayed with the thin dark-colored solid lines. The light gray hairlike lines represent samples of the navigation errors from the 200 Monte Carlo runs.

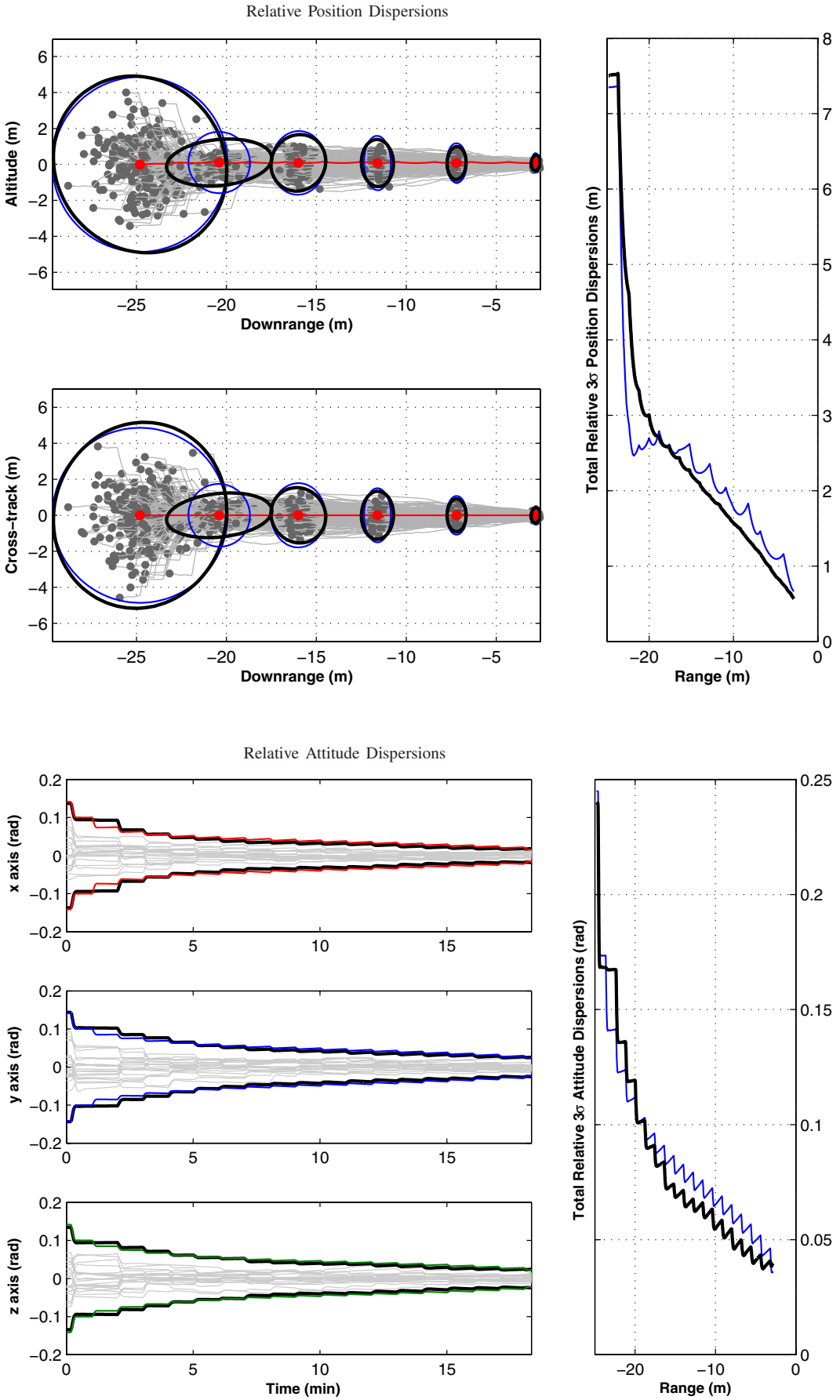

Fig. 6 Relative 3σ trajectory dispersions as a function of range along the nominal trajectory in LVLH coordinates. Relative 3σ attitude dispersions in the chaser frame are also included. The thick black ellipses (or lines) represent the statistical dispersions for 200 Monte Carlo runs. The thin dark-colored ellipses (or lines) are the dispersion, computed from the LinCov analysis. The thick line passing through the center of the error ellipses depicts the nominal trajectory. Sample dispersions from the Monte Carlo simulations are shown with light gray hairlike lines and dots.

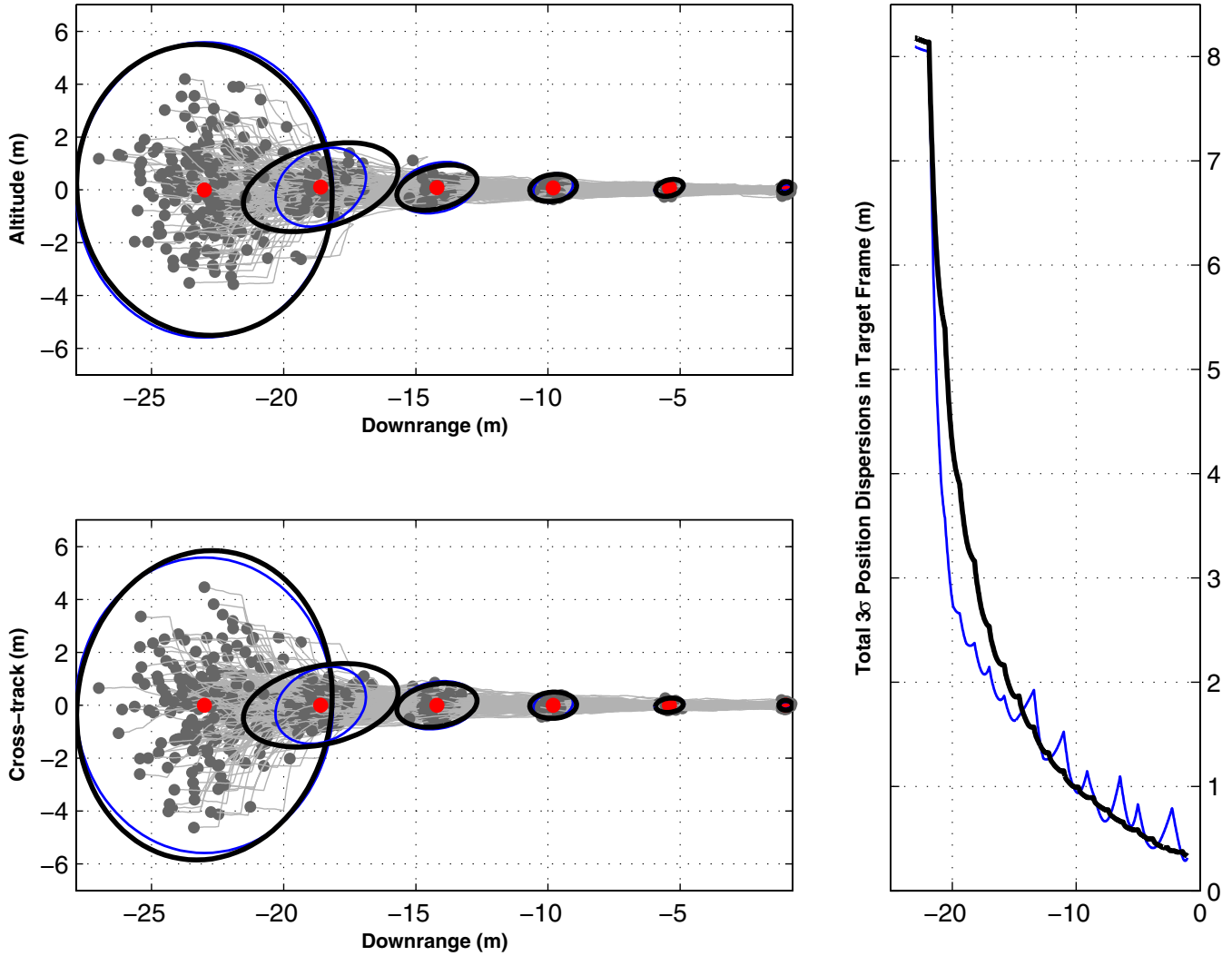

Fig. 7 Relative position dispersions between the chaser's attach point and the target's docking port in the target frame. The dispersion ellipse are plotted as a function of the nominal downrange, cross-track, and altitude directions, which coincides with the nominal target frame. The 3σ statistical results from 200 Monte Carlo simulations are shown with thick black lines and the 3σ trajectory dispersions generated by the LinCov tool are displayed with the thin dark-colored lines. The light gray hairlike lines represent samples of the trajectory dispersions from the 200 Monte Carlo runs.

C. Closed-Loop-System Analysis

Although an evaluation of the navigation system is important, it is the performance of the entire closed-loop relative position and attitude control system that must be carefully evaluated. The closed-loop analysis must include the effects of sensors, actuators, dynamics, and flight software, including navigation, guidance, and control algorithms.

The top of Fig. 6 shows the 3σ Monte Carlo and LinCov relative dispersion ellipses between the chaser and target vehicles' centers of mass along the nominal relative trajectory in LVLH coordinates. These ellipses represent the 99.74% probability dispersion bounds. The total 3σ magnitude of the relative position dispersions is also included as a function of the nominal downrange. The data show that even though the navigation errors are small (see Fig. 5), the trajectory dispersions from the nominal v-bar approach are as much as 2 m in both the cross-track and altitude directions. These dispersions are driven primarily by the desire to approach the target along its body x axis, which is in turn dispersed from the nominal local-horizontal orientation. When the attach point on the chaser vehicle is 1 m away from the target's docking port, the total 3σ value of the relative position error using Monte Carlo simulations is 57 cm and using the linear covariance analysis is 67 cm. The relative attitude dispersions are also shown in Fig. 6 with the lower plots. Unlike the impulsive Δv maneuvers, the continuous attitude control system allows the relative attitude dispersions to mimic the navigation errors (see the bottom of Fig. 5).

From a GNC viewpoint, the mission objective is to approach the object along the target's body x axis. More specifically, the objective is to move the *attach point* along the target's docking frame x axis toward the docking point. Recall that the attach point and the docking point are offset 1 and 0.8 m from their respective spacecraft's centers of mass. Thus, the key performance measure is the dispersion of the attach point from its nominal location in the target's docking frame. This single performance measure combines the effects of both relative position dispersions and relative attitude dispersions. Figure 7 shows the statistical and LinCov 3σ relative position dispersion between the attach point on the chaser vehicle and the docking port in the target frame. Note the total 3σ values of the relative position errors of the attach point at the final 1-m position. It has a 3σ value of 31 cm using the LinCov tool and 34 cm from the Monte Carlo results. These values are about half of the relative dispersion levels between the vehicles' centers of mass expressed in the LVLH frame (see the top of Fig. 6).

VI. Conclusions

The potential of angles-only navigation for autonomous orbit rendezvous is immense, especially when considered in the context of optical navigation. When taking angle measurements to target features, additional information beyond the simple line-of-sight vector can be obtained. In particular, the relative range becomes directly observable by measuring the angular separation between

features. Relative attitude can also be deduced from the measured feature geometry. This potential has been recognized in the past and now serves as a key technology for a variety of future space missions. Angles-only navigation can provide relative position and attitude information necessary for rendezvous and close-proximity operations at a lower cost in terms of mass, power, volume, and complexity than traditional methods.

The development and implementation of a prototype angles-only navigation filter in a closed-loop GNC environment confirms that relative position and attitude between two spacecraft can be determined when processing angle measurements to known features on the target. These results obtained by Monte Carlo analysis verify an earlier study using linear covariance analysis techniques. With both methods, the ultimate potential of angles-only navigation and its limitations of accurately determining relative attitude and position are observed. For the given scenario when the chaser slowly approaches the target on the v-bar, angle measurements to target features quickly eliminate cross-track and altitude errors, but they are unable to initially determine the relative range accurately. However, as the distance separating the target and chaser is reduced, the angular separation between target features becomes more detectable, allowing a better estimation of range and relative attitude. Although estimating range at large distance proves to be a challenge, there are other passive solutions to determining range, including using target features with larger separations and small maneuvers designed specifically to improve range observability. The analysis generated from both a Monte Carlo simulation and the LinCov tool also demonstrates that closed-loop relative attitude and position control performance can be achieved to provide dispersion levels that will enable rendezvous and close-proximity operations. For the proposed GNC system, when angle measurements are processed at a conservative one-minute interval, centimeter-level position dispersion to attach points when separated by 1 m is possible.

Linear covariance programs can provide Monte Carlo-like statistical results in a closed-loop GNC setting even though only a fraction of the time is required to run the analysis. The overall trends between both approaches were extremely similar, with small discrepancies in the details. This observation summarizes the strengths and weaknesses of both approaches. The speed and accuracy of linear covariance programs in determining navigation knowledge and trajectory dispersions is invaluable, especially in the early design phases of rendezvous and inspection missions. It can help untangle the complex interdependencies of a closed-loop system quickly and reliably. For a more intricate analysis of specific filter designs or various aspects of the GNC system, Monte Carlo simulations play a vital role in revealing design subtleties that may have a great affect on the overall mission. One approach gives a quick big picture of the problem, whereas the other allows a more focused and detailed view at the expense of longer simulation times. Together, they provide complementary results and serve as a tremendous analysis package that is adaptable to the needs of the entire design process.

Appendix: Navigation Equations and Matrices

I. Propagation Equations and Matrices

A. State Transition Matrix Φ

The state transition matrix used to propagate the state covariance matrix is defined as the matrix exponential $e^{F(t-t_O)}$ and approximated by expanding the exponential in a Taylor series to fourth order.[¶]

$$\boldsymbol{\Phi} = \boldsymbol{I} + \boldsymbol{F}\Delta T + \frac{\boldsymbol{F}^2\Delta T^2}{2!} + \frac{\boldsymbol{F}^3\Delta T^3}{3!} + \frac{\boldsymbol{F}^4\Delta T^4}{4!} \tag{A1}$$

The $\boldsymbol{F}$ matrix, the partial of the navigation-state dynamics with respect to the modified navigation states, has the form

$$\boldsymbol{F} = \frac{\partial \boldsymbol{f}(\hat{\boldsymbol{m}}, \hat{\boldsymbol{u}}, t)}{\partial \hat{\boldsymbol{m}}} = \begin{bmatrix} \boldsymbol{F}_{TT} & \boldsymbol{0}_{12\times 9} & \boldsymbol{0}_{12\times 9} \\ \boldsymbol{0}_{9\times 12} & \boldsymbol{F}_{CC} & \boldsymbol{F}_{CP} \\ \boldsymbol{0}_{9\times 12} & \boldsymbol{0}_{9\times 9} & \boldsymbol{F}_{PP} \end{bmatrix}$$

where the partial of the target states has the form

$$\boldsymbol{F}_{TT} = \begin{bmatrix} \boldsymbol{0}_{3\times 3} & \boldsymbol{F}_{T1} & \boldsymbol{0}_{3\times 3} & \boldsymbol{0}_{3\times 3} \\ \boldsymbol{F}_{T2} & \boldsymbol{0}_{3\times 3} & \boldsymbol{0}_{3\times 3} & \boldsymbol{0}_{3\times 3} \\ \boldsymbol{0}_{3\times 3} & \boldsymbol{0}_{3\times 3} & \boldsymbol{F}_{T3} & \boldsymbol{F}_{T4} \\ \boldsymbol{F}_{T5} & \boldsymbol{0}_{3\times 3} & \boldsymbol{F}_{T6} & \boldsymbol{F}_{T7} \end{bmatrix}$$

such that

$$\boldsymbol{F}_{T1} = \boldsymbol{I}_{3\times 3} \qquad \boldsymbol{F}_{T2} = \frac{\partial \boldsymbol{g}_T(\boldsymbol{r}_T)}{\partial \boldsymbol{r}_T} \qquad \boldsymbol{F}_{T3} = -[\hat{\boldsymbol{\omega}}_T^T\times]$$

$$\boldsymbol{F}_{T4} = \boldsymbol{I}_{3\times 3} \qquad \boldsymbol{F}_{T7} = \boldsymbol{I}_T^{-1}\{[(\boldsymbol{I}_T\hat{\boldsymbol{\omega}}_T^T)\times] - [\hat{\boldsymbol{\omega}}_T^T\times]\boldsymbol{I}_T\}$$

$$\begin{aligned}\boldsymbol{F}_{T5} = \boldsymbol{I}_T^{-1}\Bigg(&\frac{3\mu}{|\hat{\boldsymbol{r}}_T|^5}\{[\boldsymbol{T}(\hat{\boldsymbol{q}}_{I\to T})|\hat{\boldsymbol{r}}_T\times]\boldsymbol{I}_T\boldsymbol{T}(\hat{\boldsymbol{q}}_{I\to T}) \\ &- [\boldsymbol{I}_T\boldsymbol{T}(\hat{\boldsymbol{q}}_{I\to T})\hat{\boldsymbol{r}}_T\times]\boldsymbol{T}(\hat{\boldsymbol{q}}_{I\to T})\} \\ &+ \left(\frac{-15\mu}{|\hat{\boldsymbol{r}}_T|^6}\right)\boldsymbol{i}_T^T\{[\boldsymbol{T}(\hat{\boldsymbol{q}}_{I\to T})\hat{\boldsymbol{r}}_T\times]\boldsymbol{I}_T\boldsymbol{T}(\hat{\boldsymbol{q}}_{I\to T})\hat{\boldsymbol{r}}_T\}\Bigg)\end{aligned}$$

$$\begin{aligned}\boldsymbol{F}_{T6} = \boldsymbol{I}_T^{-1}&\frac{3\mu}{|\hat{\boldsymbol{r}}_T|^5}\{[\boldsymbol{T}(\hat{\boldsymbol{q}}_{I\to T})\hat{\boldsymbol{r}}_T\times]\boldsymbol{I}_T \\ &- [\boldsymbol{I}_T\boldsymbol{T}(\hat{\boldsymbol{q}}_{I\to T})\hat{\boldsymbol{r}}_T\times]\}[\boldsymbol{T}(\hat{\boldsymbol{q}}_{I\to T})\hat{\boldsymbol{r}}_T\times]\end{aligned}$$

The chaser- and parameter-state partials are

$$\boldsymbol{F}_{CC} = \begin{bmatrix} \boldsymbol{0}_{3\times 3} & \boldsymbol{F}_{C1} & \boldsymbol{0}_{3\times 3} \\ \boldsymbol{F}_{C2} & \boldsymbol{0}_{3\times 3} & \boldsymbol{0}_{3\times 3} \\ \boldsymbol{0}_{3\times 3} & \boldsymbol{0}_{3\times 3} & \boldsymbol{F}_{C3} \end{bmatrix} \qquad \boldsymbol{F}_{PP} = \begin{bmatrix} \boldsymbol{F}_{P1} & \boldsymbol{0}_{3\times 3} & \boldsymbol{0}_{3\times 3} \\ \boldsymbol{0}_{3\times 3} & \boldsymbol{F}_{P2} & \boldsymbol{0}_{3\times 3} \\ \boldsymbol{0}_{3\times 3} & \boldsymbol{0}_{3\times 3} & \boldsymbol{F}_{P3} \end{bmatrix}$$

$$\boldsymbol{F}_{CP} = \begin{bmatrix} \boldsymbol{0}_{3\times 3} & \boldsymbol{0}_{3\times 3} & \boldsymbol{0}_{3\times 3} \\ \boldsymbol{0}_{3\times 3} & \boldsymbol{0}_{3\times 3} & \boldsymbol{0}_{3\times 3} \\ \boldsymbol{F}_{CP1} & \boldsymbol{0}_{3\times 3} & \boldsymbol{0}_{3\times 3} \end{bmatrix}$$

where the partials of the chaser states are

$$\boldsymbol{F}_{C1} = \boldsymbol{I}_{3\times 3} \qquad \boldsymbol{F}_{C2} = \frac{\partial \boldsymbol{g}_C(\boldsymbol{r}_C)}{\partial \boldsymbol{r}_C} \qquad \boldsymbol{F}_{C3} = -[(\tilde{\boldsymbol{\omega}}_C^C - \hat{\boldsymbol{b}}_\omega^C)\times]$$

$$\boldsymbol{F}_{CP1} = -\boldsymbol{I}_{3\times 3}$$

and the partials of the parameter states are

$$\boldsymbol{F}_{P1} = \left(-\frac{1}{\tau_b}\right)\boldsymbol{I}_{3\times 3} \qquad \boldsymbol{F}_{P2} = \left(-\frac{1}{\tau_S}\right)\boldsymbol{I}_{3\times 3} \qquad \boldsymbol{F}_{P3} = \left(-\frac{1}{\tau_O}\right)\boldsymbol{I}_{3\times 3}$$

B. State Process-Noise Covariance Matrix $\boldsymbol{Q}_w$

The state process-noise covariance matrix represents the added uncertainty in the predicted estimate due to limitations of the mathematical models of the state dynamics. The general expression for $\boldsymbol{Q}_w$ written in integral form is

$$\boldsymbol{Q}_w = \int_{t_O}^{t} \boldsymbol{\Phi}\boldsymbol{S}_w\boldsymbol{\Phi}^T\,\mathrm{d}\tau \tag{A2}$$

where $\boldsymbol{\Phi}$ is the state transition matrix and $\boldsymbol{S}_w$ defines the strength of the *process* noise affecting each of the modified states. It has the form

$$\boldsymbol{S}_w = \begin{bmatrix} \boldsymbol{S}_{w_T} & \boldsymbol{0}_{12\times 9} & \boldsymbol{0}_{12\times 9} \\ \boldsymbol{0}_{9\times 12} & \boldsymbol{S}_{w_C} & \boldsymbol{0}_{9\times 9} \\ \boldsymbol{0}_{9\times 12} & \boldsymbol{0}_{9\times 9} & \boldsymbol{S}_{w_P} \end{bmatrix} \tag{A3}$$

where the matrix $\boldsymbol{S}_{w_T}$ characterizes the errors in the target dynamics and $\boldsymbol{S}_{w_C}$ represents the model uncertainty associated with the chaser states.

[¶]A closed-form solution for the parameter states can be derived. Also, Lear [30] generated a compact form for the state transition matrix for the position and velocity states based on a fourth-order Runge–Kutta integrator for J2 gravity.

$$\boldsymbol{S}_{w_T} = \begin{bmatrix} \boldsymbol{0}_{3\times3} & \boldsymbol{0}_{3\times3} & \boldsymbol{0}_{3\times3} & \boldsymbol{0}_{3\times3} \\ \boldsymbol{0}_{3\times3} & \sigma^2_{\dot{v}_T}\boldsymbol{I}_{3\times3} & \boldsymbol{0}_{3\times3} & \boldsymbol{0}_{3\times3} \\ \boldsymbol{0}_{3\times3} & \boldsymbol{0}_{3\times3} & \boldsymbol{0}_{3\times3} & \boldsymbol{0}_{3\times3} \\ \boldsymbol{0}_{3\times3} & \boldsymbol{0}_{3\times3} & \boldsymbol{0}_{3\times3} & \sigma^2_{\dot{\omega}_T}\boldsymbol{I}_{3\times3} \end{bmatrix} \tag{A4}$$

$$\boldsymbol{S}_{w_C} = \begin{bmatrix} \boldsymbol{0}_{3\times3} & \boldsymbol{0}_{3\times3} & \boldsymbol{0}_{3\times3} \\ \boldsymbol{0}_{3\times3} & \sigma^2_{\dot{v}_C}\boldsymbol{I}_{3\times3} & \boldsymbol{0}_{3\times3} \\ \boldsymbol{0}_{3\times3} & \boldsymbol{0}_{3\times3} & \boldsymbol{0}_{3\times3} \end{bmatrix}$$

The strength of the process noise for the parameter states $\boldsymbol{S}_{w_P}$ is defined as

$$\boldsymbol{S}_{w_P} = \begin{bmatrix} \sigma^2_b\boldsymbol{I}_{3\times3} & \boldsymbol{0}_{3\times3} & \boldsymbol{0}_{3\times3} \\ \boldsymbol{0}_{3\times3} & \sigma^2_s\boldsymbol{I}_{3\times3} & \boldsymbol{0}_{3\times3} \\ \boldsymbol{0}_{3\times3} & \boldsymbol{0}_{3\times3} & \sigma^2_o\boldsymbol{I}_{3\times3} \end{bmatrix} \tag{A5}$$

The integral in Eq. (A2) is solved by approximating the state transition matrix to first order, $\boldsymbol{\Phi} \approx \boldsymbol{I} + \boldsymbol{F}\Delta T$. The approximate value for the state process-noise covariance matrix then becomes

$$\boldsymbol{Q}_w \approx \begin{bmatrix} \boldsymbol{Q}_{w_T} & \boldsymbol{0}_{12\times9} & \boldsymbol{0}_{12\times9} \\ \boldsymbol{0}_{9\times12} & \boldsymbol{Q}_{w_C} & \boldsymbol{0}_{9\times9} \\ \boldsymbol{0}_{9\times12} & \boldsymbol{0}_{9\times9} & \boldsymbol{Q}_{w_P} \end{bmatrix} \tag{A6}$$

where $\boldsymbol{Q}_{w_T}$ represents the state process-noise covariance matrix associated with the target vehicle,

$$\boldsymbol{Q}_{w_T} = \begin{bmatrix} \sigma^2_{\dot{v}_T}\begin{bmatrix} \boldsymbol{I}\left(\frac{\Delta T^3}{3}\right) & \boldsymbol{I}\left(\frac{\Delta T^2}{2}\right) \\ \boldsymbol{I}\left(\frac{\Delta T^2}{2}\right) & \boldsymbol{I}(\Delta T) \end{bmatrix} & \boldsymbol{0}_{6\times6} \\ \boldsymbol{0}_{6\times6} & \sigma^2_{\dot{\omega}_T}\begin{bmatrix} \boldsymbol{I}\left(\frac{\Delta T^3}{3}\right) & \boldsymbol{I}\left(\frac{\Delta T^2}{2}\right) \\ \boldsymbol{I}\left(\frac{\Delta T^2}{2}\right) & \boldsymbol{I}(\Delta T) \end{bmatrix} \end{bmatrix} \tag{A7}$$

$\boldsymbol{Q}_{w_C}$ characterizes the state process-noise covariance matrix for the dynamics of the chaser vehicle,

$$\boldsymbol{Q}_{w_C} = \begin{bmatrix} \sigma^2_{\dot{v}_C}\begin{bmatrix} \boldsymbol{I}\left(\frac{\Delta T^3}{3}\right) & \boldsymbol{I}\left(\frac{\Delta T^2}{2}\right) \\ \boldsymbol{I}\left(\frac{\Delta T^2}{2}\right) & \boldsymbol{I}_{(\Delta T)} \end{bmatrix} & \boldsymbol{0}_{6\times3} \\ \boldsymbol{0}_{3\times6} & \boldsymbol{0}_{3\times3} \end{bmatrix} \tag{A8}$$

and $\boldsymbol{Q}_{w_P}$ is the noise covariance matrix of the chaser's parameters. Because of the dynamics of the parameter states, the closed-form solution can be computed.

$$\boldsymbol{Q}_{w_P} = \begin{bmatrix} \sigma^2_b(1-e^{-2\Delta T/\tau_b})\boldsymbol{I}_{3\times3} & \boldsymbol{0}_{3\times3} & \boldsymbol{0}_{3\times3} \\ \boldsymbol{0}_{3\times3} & \sigma^2_s(1-e^{-2\Delta T/\tau_s})\boldsymbol{I}_{3\times3} & \boldsymbol{0}_{3\times3} \\ \boldsymbol{0}_{3\times3} & \boldsymbol{0}_{3\times3} & \sigma^2_o(1-e^{-2\Delta T/\tau_O})\boldsymbol{I}_{3\times3} \end{bmatrix} \tag{A9}$$

C. Gyro Process-Noise Covariance Matrix $\boldsymbol{Q}_\eta$

The uncertainty introduced to the estimate of the chaser's attitude by using noisy gyro measurements is represented with $\boldsymbol{Q}_\eta$. It is approximated as the product of the strength of the gyro random angular walk and the time step.

$$\boldsymbol{Q}_\eta \approx \boldsymbol{S}_\eta \Delta T \tag{A10}$$

II. Update Equations and Matrices

A. Optical-Camera-Feature Measurements

The flight computer's estimate of the angle measurements of the target features is based on the model in Eqs. (23) and (24).

$$\hat{\boldsymbol{h}}_F(\hat{\boldsymbol{x}}) = \begin{bmatrix} \hat{h}_\alpha(\hat{\boldsymbol{x}}) \\ \hat{h}_e(\hat{\boldsymbol{x}}) \end{bmatrix} = \begin{bmatrix} \hat{\alpha} \\ \hat{e} \end{bmatrix} = \begin{bmatrix} \tan^{-1}\left(\frac{i_y}{i_x}\right) \\ \sin^{-1}(i_z) \end{bmatrix} \tag{A11}$$

where $[i_x \;\; i_y \;\; i_z]^T$ are the individual components of the relative line-of-sight unit vector $\boldsymbol{i}^O_\rho$ between the optical camera and the target (or target features) represented in the optical frame. The measurement sensitivity matrix for the relative measurements to a feature of the target is defined as

$$\hat{\boldsymbol{H}}_F = \frac{\partial \hat{\boldsymbol{h}}_F(\hat{\boldsymbol{x}})}{\partial \hat{\boldsymbol{x}}} = \begin{bmatrix} \hat{\boldsymbol{h}}_\alpha \\ \hat{\boldsymbol{h}}_e \end{bmatrix} \tag{A12}$$

where the measurement partials for the azimuth and elevation measurements to a target feature equal

$$\hat{\boldsymbol{h}}_\alpha = \frac{\partial \hat{h}_\alpha(\hat{\boldsymbol{x}})}{\partial \hat{\boldsymbol{x}}} \tag{A13}$$

$$\hat{\boldsymbol{h}}_e = \frac{\partial \hat{h}_e(\hat{\boldsymbol{x}})}{\partial \hat{\boldsymbol{x}}} \tag{A14}$$

Theoretically, from the nonlinear measurement equations (A11), the measurement sensitivity matrix can be derived. Another method that proves to be more efficient and practical computes the measurement partial using the chain rule and the relative range vector $\hat{\boldsymbol{\rho}}^O$. Note that the range vector in the optical camera frame can be expressed as a function of the measurements and states.

$$\hat{\boldsymbol{\rho}}^O = \hat{\rho}\begin{bmatrix} \cos(\hat{e})\cos(\hat{\alpha}) \\ \cos(\hat{e})\sin(\hat{\alpha}) \\ \sin(\hat{e}) \end{bmatrix} \tag{A15}$$

$$\hat{\boldsymbol{\rho}}^O = [(\boldsymbol{I} - [\hat{\boldsymbol{\epsilon}}^O_O\times])\boldsymbol{T}_{C\to\hat{O}}(\boldsymbol{I} - [\hat{\boldsymbol{\theta}}^C_C\times])\boldsymbol{T}_{I\to\hat{C}}]([\hat{\boldsymbol{r}}_T + \hat{\boldsymbol{r}}_F] - [\hat{\boldsymbol{r}}_C + \hat{\boldsymbol{r}}_O]) \tag{A16}$$

Using the chain rule, the partial of the relative range vector with respect to the navigation states can be expressed as

$$\frac{\partial \hat{\boldsymbol{\rho}}^O}{\partial \hat{\boldsymbol{x}}} = \frac{\partial \hat{\boldsymbol{\rho}}^O}{\partial \hat{\alpha}}\frac{\partial \hat{h}_\alpha}{\partial \hat{\boldsymbol{x}}} + \frac{\partial \hat{\boldsymbol{\rho}}^O}{\partial \hat{e}}\frac{\partial \hat{h}_e}{\partial \hat{\boldsymbol{x}}}$$

where the measurement geometry vectors naturally emerge when evaluating the partials associated with the chain rule.

$$\frac{\partial \hat{\boldsymbol{\rho}}^O}{\partial \hat{\boldsymbol{x}}} = (\rho \mathbf{p}^O_\alpha)\hat{\boldsymbol{h}}_\alpha + (\rho \mathbf{p}^O_e)\hat{\boldsymbol{h}}_e \tag{A17}$$

The vectors $\mathbf{p}^O_\alpha$ and $\mathbf{p}^O_e$ represent the partials of the line-of-sight unit vector to the target in the camera frame with respect to the azimuth and elevation measurements, respectively.

$$\mathbf{p}^O_\alpha = \begin{bmatrix} -\cos(\hat{e})\sin(\hat{\alpha}) \\ \cos(\hat{e})\cos(\hat{\alpha}) \\ 0 \end{bmatrix} \qquad \mathbf{p}^O_e = \begin{bmatrix} -\sin(\hat{e})\cos(\hat{\alpha}) \\ -\sin(\hat{e})\sin(\hat{\alpha}) \\ \cos(\hat{e}) \end{bmatrix}$$

The measurement geometry vectors can now be computed by taking advantage of the property that the vectors $\mathbf{p}^O_\alpha$ and $\mathbf{p}^O_e$ are orthogonal to one another and taking the dot product with respect to each.

$$\hat{\boldsymbol{h}}_\alpha = \frac{(\mathbf{p}^O_\alpha)^T}{\hat{\rho}\cos^2(\hat{e})}\left[\frac{\partial \hat{\boldsymbol{\rho}}^O}{\partial \hat{\boldsymbol{x}}}\right] \tag{A18}$$

$$\hat{\boldsymbol{h}}_e = \frac{(\mathbf{p}^O_e)^T}{\hat{\rho}}\left[\frac{\partial \hat{\boldsymbol{\rho}}^O}{\partial \hat{\boldsymbol{x}}}\right] \tag{A19}$$

Evaluating the partial of the relative range vector with respect to the navigation states yields

$$\left[\frac{\partial \hat{\boldsymbol{\rho}}^O}{\partial \hat{\boldsymbol{x}}}\right] = [\boldsymbol{T}_{I\to O}\ \ \boldsymbol{0}_{3\times 3}\ \ -\boldsymbol{T}_{T\to O}(\boldsymbol{r}_F^T\times)\ \ \boldsymbol{0}_{3\times 3} \\ -\boldsymbol{T}_{I\to O}\ \ \boldsymbol{0}_{3\times 3}\ \ \boldsymbol{T}_{C\to O}[(\boldsymbol{r}_T^C+\boldsymbol{r}_F^C-\boldsymbol{r}_C^C)\times]\ \ \boldsymbol{0}_{3\times 3}\ \ \boldsymbol{0}_{3\times 3}\ \ (\boldsymbol{\rho}^O\times)] \tag{A20}$$

which gives the final expression for the measurement sensitivities for azimuth and elevation measurements when substituted into Eqs. (A18) and (A19).

$$\hat{\boldsymbol{h}}_\alpha = \frac{1}{\hat{\rho}\cos^2(\hat{e})}[\mathbf{p}_\alpha^I\ \ \boldsymbol{0}_{1\times 3}\ \ -\mathbf{p}_\alpha^T\times\boldsymbol{r}_F^T\ \ \boldsymbol{0}_{1\times 3}\ \ -\mathbf{p}_\alpha^I\ \ \boldsymbol{0}_{1\times 3}\ \ \mathbf{p}_\alpha^C \\ \times(\boldsymbol{r}_T^C+\boldsymbol{r}_F^C-\boldsymbol{r}_C^C)\ \ \boldsymbol{0}_{1\times 6}\ \ \mathbf{p}_\alpha^O\times\boldsymbol{\rho}^O] \tag{A21}$$

$$\hat{\boldsymbol{h}}_e = \frac{1}{\hat{\rho}}[\mathbf{p}_e^I\ \ \boldsymbol{0}_{1\times 3}\ \ -\mathbf{p}_e^T\times\boldsymbol{r}_F^T\ \ \boldsymbol{0}_{1\times 3}\ \ -\mathbf{p}_e^I\ \ \boldsymbol{0}_{1\times 3}\ \ \mathbf{p}_e^C \\ \times(\boldsymbol{r}_T^C+\boldsymbol{r}_F^C-\boldsymbol{r}_C^C)\ \ \boldsymbol{0}_{1\times 6}\ \ \mathbf{p}_e^O\times\boldsymbol{\rho}^O] \tag{A22}$$

The flight computer's value of the optical camera measurement covariance is

$$\boldsymbol{R}_O = \begin{bmatrix}\sigma_{o_x} & 0\\ 0 & \sigma_{o_y}\end{bmatrix} \tag{A23}$$

B. Star-Camera Measurements

When processing star-camera data, a *derived* measurement [31] is calculated. It is effectively the residual to be processed by the Kalman filter.

$$\begin{bmatrix}\frac{1}{2}\tilde{\boldsymbol{z}}_s\\ 1\end{bmatrix} = \tilde{\boldsymbol{q}}_{I\to\tilde{S}}\otimes[\hat{\boldsymbol{q}}_{C\to I}\otimes\hat{\boldsymbol{q}}_{S\to C}\otimes\delta\boldsymbol{q}(\hat{\boldsymbol{\epsilon}}_S^S)] \tag{A24}$$

The flight computer's estimate of the derived star-camera measurement is a function of the modified state rotation vector $\hat{\boldsymbol{\theta}}_C^C$, and the camera misalignment is $\hat{\boldsymbol{\epsilon}}_S^S$.

$$\hat{\boldsymbol{h}}_S(\hat{\boldsymbol{x}}) = \boldsymbol{T}(\hat{\boldsymbol{q}}_{C\to S})\hat{\boldsymbol{\theta}}_C^C + \hat{\boldsymbol{\epsilon}}_S^S \tag{A25}$$

The measurement sensitivity matrix for the star camera is given by

$$\boldsymbol{H}_S = [\boldsymbol{0}_{3\times 12}\ \ \boldsymbol{0}_{3\times 6}\ \ \boldsymbol{T}(\hat{\boldsymbol{q}}_{C\to S})\ \ \boldsymbol{0}_{3\times 3}\ \ \boldsymbol{I}_{3\times 3}\ \ \boldsymbol{0}_{3\times 3}] \tag{A26}$$

and the flight computer's value of the star-camera measurement covariance is

$$\boldsymbol{R}_S = \begin{bmatrix}\sigma_{s_x} & 0 & 0\\ 0 & \sigma_{s_y} & 0\\ 0 & 0 & \sigma_{s_z}\end{bmatrix} \tag{A27}$$

III. Correction Equations and Matrices

The correction of the navigation-state covariance in Eq. (45) is accomplished using the following partial derivative.

$$\hat{\boldsymbol{D}} = \begin{bmatrix}\boldsymbol{0}_{12\times 12} & \boldsymbol{0}_{12\times 9} & \boldsymbol{0}_{12\times 9}\\ \boldsymbol{0}_{9\times 12} & \hat{\boldsymbol{D}}_C & \boldsymbol{0}_{9\times 9}\\ \boldsymbol{0}_{9\times 12} & \boldsymbol{0}_{9\times 9} & \boldsymbol{0}_{9\times 9}\end{bmatrix} \tag{A28}$$

where

$$\hat{\boldsymbol{D}}_C = \begin{bmatrix}\boldsymbol{0}_{3\times 3} & \boldsymbol{0}_{3\times 3} & \boldsymbol{0}_{3\times 3}\\ \boldsymbol{0}_{3\times 3} & \boldsymbol{0}_{3\times 3} & \partial\hat{\boldsymbol{u}}_{\Delta v}/\partial\hat{\boldsymbol{\theta}}_C^C\\ \boldsymbol{0}_{3\times 3} & \boldsymbol{0}_{3\times 3} & \boldsymbol{0}_{3\times 3}\end{bmatrix}$$

and the partial of the Δv maneuver with respect to the modified chaser-attitude state equals

$$\frac{\partial\hat{\boldsymbol{u}}_{\Delta v}}{\partial\hat{\boldsymbol{\theta}}_C^C} = \boldsymbol{T}(\hat{\boldsymbol{q}}_{C\to I})[\Delta\hat{\boldsymbol{v}}_{\text{cmd}}^C\times] \tag{A29}$$

References

[1] Polites, M. E., "An Assessment of the Technology of Automated Rendezvous and Capture in Space," NASA Marshall Space Flight Center Paper TP-1998-208528, July 1998.

[2] Kim, S., Crassidis J. L., Cheng, Y., and Fosbury, A. M., "Kalman Filtering for Relative Spacecraft Attitude and Position Estimation," *Journal of Guidance, Control, and Dynamics*, Vol. 30, No. 1, 2007, pp. 133–143.

[3] Yim, J. R., Crassidis J. L., and Junkins, J. L., "Autonomous Orbit Navigation of Two Spacecraft System Using Relative Line of Sight Vector Measurements," American Astronautical Society Paper 04-257, 2004.

[4] Junkins, J. L., Hughes, D. C., Wazni, K. P., and Pariyapong, V., "Vision-Based Navigation for Rendezvous and Docking and Proximity Operations," 22nd Annual AAS Guidance and Control Conference, Breckenridge, CO, American Astronautical Society Paper 99-021, 1999.

[5] Howard, R. T., and Bryan, T. C., "Video Guidance Sensor for Automated Capture," Space Programs and Technologies Conference, Huntsville, AL, AIAA Paper 1992-1389, 1992.

[6] Howard, R. T., Bryan, T. C., and Book, M. L., "On-Orbit Testing of the Video Guidance Sensor," *Proceedings of SPIE*, Vol. 3707, SPIE—The International Society for Optical Engineering, Bellingham, WA, May 1999, pp. 290–300.

[7] Mukundan, R., Narayanan, R. R., and Philip, N., "A Vision Based Attitude and Position Estimation Algorithm for Rendezvous and Docking," *Journal of Spacecraft Technology: Windows Magazine*, Vol. 4, No. 2, July 1994, pp. 60–66.

[8] Abidi, M., and Chandra, T., "A New Efficient and Direct Solution for Pose Estimation Using Quadrangular Targets: Algorithm and Evaluation," *IEEE Transactions on Pattern Analysis and Machine Intelligence*, Vol. 17, No. 5, May 1995, pp. 534–538.

[9] Geller, D. K., "Analysis of the Relative Attitude Estimation and Control Problem for Satellite Inspection and Orbital Rendezvous," *Journal of the Astronautical Sciences* (to be published).

[10] Monahan, R. D., "The Optimal Maneuver for Bearings Only Target Tracking," M.S. Thesis, Royal Military College of Canada, Kingston, Ontario, Canada, Apr. 1994.

[11] Nardone, S. C., and Graham, M. L., "A closed-form Solution to Bearings-Only Target Motion Analysis," *IEEE Journal of Oceanic Engineering*, Vol. 22, No. 1, Jan. 1997, pp. 168–178.

[12] Ristic, B., and Arulampalam, M. S., "Tracking a Manoeuvering Target Using Angle-Only Measurements: Algorithms and Performance," *Signal Processing*, Vol. 83, No. 6, 2003, pp. 1223–1238.

[13] Sabol, C., and Vallado, D., "A Fresh Look at Angles-Only Orbit Determination," AS/AIAA Astrodynamics Specialist Conference, Girdwood, AK, American Astronautical Society Paper 99-363, Aug. 1999.

[14] Gauss, C. F., *Theoria Motus: Theory of the Motion of the Heavenly Bodies Moving About the Sun in Conic Sections*, edited by C. H. Davis, Little Brown, Boston, 1857.

[15] Aidala, V. J., "Kalman Filter Behavior in Bearings-Only Tracking Applications," *IEEE Transactions on Aerospace and Electronic Systems*, Vol. AES-15, No. 1, Jan. 1979, pp. 29–39.

[16] Aidala, V. J., and Hammel, S. E., "Utilization of Modified Polar Coordinates for Bearings-Only Tracking," *IEEE Transactions on Automatic Control*, Vol. AC-28, No. 3, Mar. 1983, pp. 283–294.

[17] Blackman, S., and Popoli, R., *Design and Analysis of Modern Tracking Systems*, Artech House, Norwood, MA, 1999.

[18] Cadre, J.-P. L., and Trémois O., "Bearings-Only Tracking for Maneuvering Sources," *IEEE Transactions on Aerospace and Electronic Systems*, Vol. 34, No. 1, Jan. 1998, pp. 179–192.

[19] Hammel, S. E., "Optimal Observer Motion for Bearings-Only Localization and Tracking," Ph.D. Thesis Univ. of Rhode Island, Kingston, RI, 1988.

[20] Tuckness, D. G., and Young, S.-Y., "Autonomous Navigation for Lunar Transfer," *Journal of Spacecraft and Rockets*, Vol. 32, No. 2, Mar.–Apr. 1995, pp. 770–784.

[21] Bhaskaran, S., Riedel, J., Synnott, S., and Wang, T., "The Deep Space 1 Autonomous Navigation System: A Post- Flight Analysis," AIAA/AAS Astrodynamics Specialist Conference, AIAA Paper 2000-3935, 2000.

[22] Johnson, E., Calise, A., Watanabe, Y., Ha, J., and Neidhoefer, J., "Real-Time Vision-Based Relative Navigation," AIAA Guidance, Navigation, and Control Conference, Keystone, CO, AIAA Paper 2006-6608, 2006.

[23] Rosa, D. D., and Curti, F., "Visual Monitoring of Space Rendezvous: A Structure from Motion Problem," AIAA Guidance, Navigation, and Control Conference, Keystone, CO, AIAA Paper 2006-6762, 2006.

[24] Kawaguichi, J., Hashimoto, T., Kubota, T., and Sawai, S., "Autonomous Optical Guidance and Navigation Strategy Around a Small Body," *Journal of Guidance, Control, and Dynamics*, Vol. 20, No. 5, Sept.–Oct. 1997, pp. 1010–1017.

[25] Riedel, J., Bhaskaran, S., Eldred, D., Gaskell, R., Grasso, C., Kennedy, B., Kubitschek, D., Mastrodemos, N., Synnott, S., Vaughan, A., and Werner, R., "AutoNav Mark3: Engineering the Next Generation of Autonomous Onboard Navigation and Guidance," AIAA Guidance, Navigation, and Control Conference, Keystone, CO, AIAA Paper 2006-6708, 2006.

[26] Fehse, W., *Automated Rendezvous and Docking of Spacecraft*, Cambridge Univ. Press, Cambridge, England, U.K., 2003.

[27] Aldrin, E. E., "Line-Of-Sight Guidance Techniques for Manned Orbital Rendezvous," Ph.D. Thesis Massachusetts Inst. of Technology, Cambridge, MA, Jan. 1963.

[28] Calhoun, P. C., "Solution to the Problem of Determining the Relative 6 DOF State for Spacecraft Automated Rendezvous and Docking," *Proceedings of SPIE*, Vol. 2466, SPIE—The International Society for Optical Engineering, Bellingham, WA, 1995, pp. 175–184.

[29] Kaplan, M. H., *Modern Spacecraft Dynamics and Control*, Wiley, New York, 1976.

[30] Lear, W. M., *Kalman Filtering Techniques*, NASA Johnson Space Center: Mission Planning and Analysis Division, Houston, TX, Sept. 1985, JSC-20688.

[31] Pittelkau, M. E., "Rotation Vector in Attitude Estimation," *Journal of Guidance, Control, and Dynamics*, Vol. 26, No. 6, Nov.–Dec. 2003, pp. 855–859.

[32] Wertz, J. R., *Spacecraft Attitude Determination and Control*, 1st ed, Astrophysics and Space Science Library, Vol. 73, D. Reidel, Dordrecht, Holland, The Netherlands, 1978.

[33] Lefferts, E., Markley, F., and Shuster, M., "Kalman Filtering for Spacecraft Attitude Estimation," *Journal of Guidance, Control, and Dynamics*, Vol. 5, No. 5, Sept.–Oct. 1982, pp. 417–429.

[34] Geller, D. K., "Linear Covariance Techniques for Orbital Rendezvous Analysis and Autonomous Onboard Mission Planning," *Journal of Guidance, Control, and Dynamics*, Vol. 29, No. 6, 2005, pp. 1404–1414.